Published for SISSA by Springer

Received: *May 9, 2025*
Accepted: *June 20, 2025*
Published: *July 17, 2025*

Measurement of the branching fraction ratio R_K at large dilepton invariant mass

The LHCb collaboration

E-mail: dl225@ic.ac.uk

Abstract: A test of lepton universality between muons and electrons is performed using $B^+ \to K^+\ell^+\ell^-$ decays (where $\ell = e, \mu$), in the dilepton invariant-mass-squared region above $14.3\,\text{GeV}^2/c^4$. The data used for the measurement consists of beauty meson decays produced in proton-proton collisions, corresponding to an integrated luminosity of $9\,\text{fb}^{-1}$, collected by the LHCb experiment between 2011 and 2018. The ratio of branching fractions for $B^+ \to K^+\mu^+\mu^-$ and $B^+ \to K^+e^+e^-$ decays is measured to be $R_K = 1.08^{+0.11}_{-0.09}$ (stat) $^{+0.04}_{-0.04}$ (syst), which is consistent with the Standard Model prediction of unity. This constitutes the most precise test of lepton flavour universality using $B^+ \to K^+\ell^+\ell^-$ decays with dilepton invariant-mass-squared above the $\psi(2S)$ mass, whilst being the first of its kind at a hadron collider.

Keywords: Flavour Changing Neutral Currents, Flavour Physics, B Physics, Hadron-Hadron Scattering

ArXiv ePrint: 2505.03483

Open Access, Copyright CERN, for the benefit of the LHCb Collaboration. Article funded by SCOAP^3.

https://doi.org/10.1007/JHEP07(2025)198

Contents

1 Introduction

The decay of a b quark to an s quark and two oppositely charged leptons ($b\to s\ell^+\ell^-$) is an example of a flavour-changing neutral current transition. In the Standard Model (SM), such processes are loop-induced because no SM gauge boson mediates the decay at tree level. Processes involving a $b\to s\ell^+\ell^-$ transition, such as $B\to K^{(*)}\ell^+\ell^-$ and $B^0_s\to\phi\mu^+\mu^-$ decays,[1] are therefore exceedingly rare with branching fractions of order $\mathcal{O}(10^{-7})$. Extensions to the SM often hypothesise the existence of new particles that are not directly detectable with current experimental resources but can contribute sizeable modifications to the properties of $b\to s\ell^+\ell^-$ transitions [1–5]. Discrepancies with respect to the SM prediction ranging from 2σ to 4σ have been observed in the measurements of branching fractions and angular observables for the decays $B^0_s\to\phi\mu^+\mu^-$, $B^+\to K^+\mu^+\mu^-$ and $B^0\to K^*(892)^0\mu^+\mu^-$ [6–11].

Calculating SM predictions for $b\to s\ell^+\ell^-$ transitions requires an understanding of hadronic form factors [12, 13] and nonperturbative long-distance effects [14], both of which are known imprecisely, complicating the interpretation of the discrepancies. However, observables involving ratios of $b\to s\ell^+\ell^-$ branching fractions for two different lepton flavours have minimal hadronic theory uncertainty, as they cancel out because the strong force does not couple to leptons. Furthermore, the Yukawa couplings for the leptons are small compared to their SM gauge couplings, leading to an accidental symmetry known as lepton universality (LU). This principle has been tested across various processes [15–18], and is most precisely confirmed in Z boson decays at the per mille level [19]. Consequently, ratios of branching fractions involving $b\to s\ell^+\ell^-$ transitions only deviate from unity due to mass-related phase-space and QED effects, which are small for ratios involving light leptons. In particular, QED effects are below 1% at dilepton invariant mass squared (q^2) lower than $6\,\text{GeV}^2/c^4$ [20] and up to 4% at q^2 above the $\psi(2S)$ resonance. These effects have been shown to be correctly modelled in the whole accessible phase space by the simulation software employed [20, 21]. Measuring

[1] In this paper, the inclusion of the charge-conjugate mode is implied.

JHEP07(2025)198

ratios of branching fractions is further motivated by an interest in beyond Standard Model theories that introduce LU-violating extensions [22–24].

Decays involving electrons or muons in the final state, rather than taus, are most commonly studied due to their experimental accessibility. Tests of LU have been conducted by the BaBar [25], Belle [26], CMS [27] and LHCb collaborations [28–33] using a wide variety of decay channels involving $b \to s\ell^+\ell^-$ transitions, yielding results that are consistent with SM expectation. The most precise LU measurements involving $B^+ \to K^+\ell^+\ell^-$ decays have been performed in the q^2 region below the J/ψ resonance, with a precision of 4% [29, 30], while the only existing LU measurement of $B^+ \to K^+\ell^+\ell^-$ in the high-q^2 region is that performed by the Belle collaboration [26]. Measurements in the high-q^2 region, above the $\psi(2S)$ resonance, are complementary to low-q^2 measurements having different background and efficiency considerations.

This paper describes a test of LU in the decays of $B^+ \to K^+\mu^+\mu^-$ and $B^+ \to K^+e^+e^-$ performed by measuring the branching fraction ratio

$$R_K \equiv \frac{\displaystyle\int_{q^2_{\rm min}}^{q^2_{\rm max}} \frac{{\rm d}\mathcal{B}(B^+ \to K^+\mu^+\mu^-)}{{\rm d}q^2}{\rm d}q^2}{\displaystyle\int_{q^2_{\rm min}}^{q^2_{\rm max}} \frac{{\rm d}\mathcal{B}(B^+ \to K^+e^+e^-)}{{\rm d}q^2}{\rm d}q^2}, \tag{1.1}$$

where the integral limits define the q^2 bin of the measurement, which for this analysis corresponds to $q^2 > 14.3\,{\rm GeV}^2/c^4$. The measurement is performed using a dataset corresponding to $9\,{\rm fb}^{-1}$ of integrated luminosity collected by the LHCb experiment between 2011 and 2018. Similar to other LU ratios in this system, the measurement is performed relative to the normalisation mode $B^+ \to K^+J/\psi(\to \ell^+\ell^-)$ in order to cancel and control many systematic uncertainties associated with the computation of efficiencies. The measured yield of $B^+ \to K^+e^+e^-$ decays was kept blind until the analysis was finalised to avoid experimenter's bias.

This paper is structured as follows: the LHCb detector and simulation are outlined in section 2. The selection requirements used to isolate signal decays, including details on how backgrounds such as $B^+ \to K^+\psi(2S)(\to e^+e^-)$ leakage are suppressed to negligible levels, are presented in section 3. In section 4, the corrections to the simulation samples and associated cross-checks are detailed. A novel method of extracting R_K that significantly reduces systematic uncertainties related to the imprecisely understood shape of the high-q^2 spectrum is presented in section 5, along with the determination of the rare $B^+ \to K^+\ell^+\ell^-$ muon and electron channel yields. Systematic uncertainties are discussed in section 6, and the result is presented in section 7.

2 Detector and simulation

The LHCb detector [34, 35] is a single-arm forward spectrometer covering the pseudorapidity range $2 < \eta < 5$, designed for the study of particles containing b or c quarks. The detector includes a high-precision tracking system consisting of a silicon-strip vertex detector surrounding the pp interaction region [36], a large-area silicon-strip detector located upstream of a dipole magnet with a bending power of about $4\,{\rm T\,m}$, and three stations of silicon-strip

JHEP07(2025)198

detectors and straw drift tubes [37, 38] placed downstream of the magnet. The tracking system provides a measurement of the momentum, p, of charged particles with a relative uncertainty that varies from 0.5% at low momentum to 1.0% at 200 GeV/c. The minimum distance of a track to a primary pp collision vertex (PV), the impact parameter, is measured with a resolution of $(15 + 29/p_{\mathrm{T}})$ µm, where p_{T} is the component of the momentum transverse to the beam, in GeV/c. Different types of charged hadrons are distinguished using information from two ring-imaging Cherenkov detectors (RICH) [39]. Photons, electrons and hadrons are identified by a calorimeter system consisting of scintillating-pad and preshower detectors, as well as an electromagnetic calorimeter (ECAL) and a hadronic calorimeter (HCAL). Muons are identified by a system composed of alternating layers of iron and multiwire proportional chambers [40]. The online event selection is performed by a trigger [41], which consists of a hardware stage, based on information from the calorimeter and muon systems, followed by a software stage, which applies a full event reconstruction.

Simulated events are used to optimise the signal selection, model the signal and backgrounds, and calculate the relative efficiency between the signal and normalisation channels. In the simulation, pp collisions are generated using Pythia [42] with a specific LHCb configuration [43]. Decays of hadronic particles are described by EvtGen [44], in which final-state radiation is generated using Photos [45]. The interaction of the generated particles with the detector and its response are implemented using the Geant4 toolkit [46] as described in ref. [47].

3 Selection

Selection requirements are applied to the data in order to isolate the signal and reduce background contamination using both the ROOT framework [48, 49] and the Scikit-HEP ecosystem [50–55] including zfit [56, 57]. Background contributions fall into two broad categories: combinatorial candidates, whereby the combined tracks do not originate from a common particle decay, and decays where tracks, despite originating from a common source, are incorrectly reconstructed by missing and/or misidentifying particles.

Since both muon and electron final states consist of three tracks originating from the same decay vertex, there is significant overlap in the requirements applied to their topological and geometric properties. In the following, the areas where the selection requirements differ between the muon and electron data are described.

Events are selected based on the decision of a hardware trigger algorithm. For the muon mode candidates, a high-p_{T} muon is required as measured using information from the muon stations. For the electron mode candidates, an electron with high transverse energy is required, defined as $E_{\mathrm{T}} = E \sin\theta$, where E is the measured energy in a cluster of cells in the ECAL, and θ is the angle between the beam direction and the line connecting the PV to the ECAL cell cluster. In a subsequent trigger stage, final-state particles satisfying minimum p_{T} and impact parameter requirements are then combined to construct $B^+ \to K^+\ell^+\ell^-$ candidates. Each candidate is required to form a good-quality vertex with a significant displacement from the primary pp collisions. To reduce contamination from misidentified backgrounds such as $B^+ \to K^+\pi^+\pi^-$ decays, a tight selection is made on particle identification (PID) variables constructed using information from all relevant subdetectors.

JHEP07(2025)198

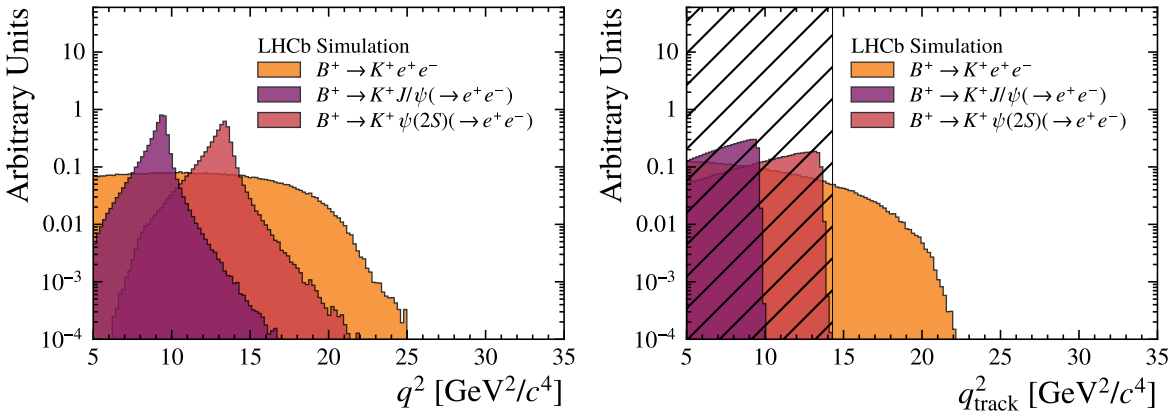

Figure 1. Normalised distributions of (left) q^2 and (right) $q^2_{\rm track}$ for simulated nonresonant $B^+ \to K^+ e^+ e^-$ signal, and the resonant decays $B^+ \to K^+ J/\psi(\to e^+ e^-)$ and $B^+ \to K^+ \psi(2S)(\to e^+ e^-)$. The hatched region illustrates the impact of the $q^2_{\rm track}$ selection.

While the identification of kaon and muon candidates employs information from the RICH detectors, the HCAL and the muon chambers, the identification of electrons relies principally on the measured ratio of energy deposited in showers in the ECAL and the reconstructed momenta of associated tracks [58]. The significantly higher likelihood for electrons to emit bremsstrahlung radiation whilst traversing the detector strongly affects their momentum resolution. To mitigate this effect, a recovery algorithm [59] searches the extrapolated track position of electrons in the ECAL for photon energy deposits not associated with any other charged tracks. Energy deposits with $E_{\rm T} > 75\,{\rm MeV}$ are added to the electron's momentum, and the reconstructed dilepton invariant mass is computed with these photon contributions included. However, incorrectly assigning bremsstrahlung deposits to electrons from $B^+ \to K^+ J/\psi(\to e^+ e^-)$ and $B^+ \to K^+ \psi(2S)(\to e^+ e^-)$ decays results in candidates from these channels leaking upwards into the nonresonant high-q^2 region, as depicted on the left-hand side of figure 1. Using the requirement $q^2 > 14.3\,{\rm GeV}^2/c^4$ to isolate the high-q^2 region would result in an unmanageable $B^+ \to K^+ \psi(2S)(\to e^+ e^-)$ background. However, the selection requirement $q^2_{\rm track} > 14.3\,{\rm GeV}^2/c^4$, where $q^2_{\rm track}$ is computed using momenta estimated by the tracking system only, reduces the background from $B^+ \to K^+ \psi(2S)(\to e^+ e^-)$ decays to negligible levels, as illustrated on the right-hand side of figure 1. Selecting candidates with the $q^2_{\rm track}$ variable, rather than q^2, approximately halves the expected number of rare $B^+ \to K^+ e^+ e^-$ candidates. Despite this, there is an improvement in the R_K precision in this higher purity selection, and hence using $q^2_{\rm track}$ is the adopted selection strategy. To ensure efficiency-related systematic uncertainties associated with modelling the resolution in the simulation cancel out, the normalisation is performed relative to the $B^+ \to K^+ J/\psi(\to e^+ e^-)$ control mode, which is also selected using the $q^2_{\rm track}$ variable. Radiative bremsstrahlung losses for muons are insignificant compared to electrons. Therefore, the bremsstrahlung recovery procedure is not used for the reconstruction of muonic final states.

Semileptonic $b \to c$ decays followed by the subsequent decay of the intermediate charm hadron form a significant source of partially reconstructed background as such channels have branching fractions orders of magnitude higher than the signal. There exists a plethora of such

JHEP07(2025)198

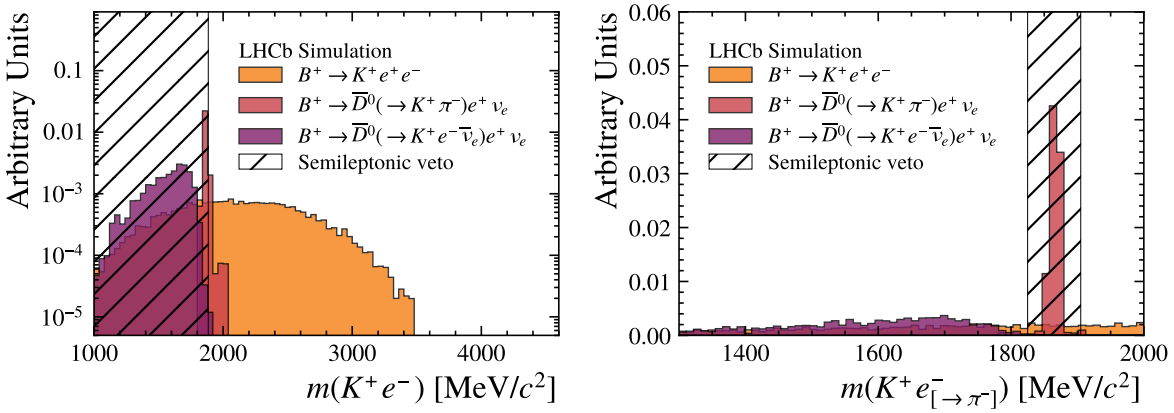

Figure 2. Normalised distributions of (left) $m(K^+e^-)$ and (right) $m(K^+e^-_{[\to\pi^-]})$ for simulated $B^+ \to K^+e^+e^-$ decays and the most significant semileptonic decay background channels. The regions that are vetoed are indicated by the hatched region.

channels which can be split into two classes depending on whether any final-state particles have been misidentified. Both classes are efficiently removed with two selection criteria, $m(K^+\ell^-) > 1885\,\text{MeV}/c^2$ and a D-mass window cut of $m(K^+\ell^-_{[\to\pi^-]}) \notin m(D^0) \pm 40\,\text{MeV}/c^2$, where $m(D^0)$ denotes the known D^0 mass [60]. The variable $m(K^+\ell^-_{[\to\pi^-]})$ is computed by assigning the pion mass hypothesis to the lepton and ignoring contributions from the bremsstrahlung recovery algorithm. The impact of these cuts on signal and background simulation samples in the electron mode is shown in figure 2.

Boosted Decision Tree (BDT) [61] classifiers are trained to distinguish $B^+ \to K^+\ell^+\ell^-$ signal decays from combinatorial background. The classification is achieved by exploiting differences in the distributions of various vertex-quality and kinematic variables between signal and combinatorial candidates. Additionally, quantities that relate to how isolated the candidate is from other particles in the event are utilised. The samples used to train the BDT classifier include simulation samples to represent signal decays and selected candidates in the data with $m(K^+\ell^+\ell^-) > 5400\,\text{MeV}/c^2$ to represent the combinatorial background. Separate BDT classifiers are trained for the muon and electron channels.

In the electron channel, a further BDT classifier is trained to reject partially reconstructed decays of the type $B^0 \to K^*(892)^0(\to K^+\pi^-)e^+e^-$ and $B^+ \to K^*(892)^+(\to K^+\pi^0)e^+e^-$, where the pion is not reconstructed. The BDT classifier is trained with features similar to the combinatorial BDT classifier; however, the background is represented by simulated partially reconstructed decays. This classifier is most effective at suppressing partially reconstructed candidates with missing charged particles since charged particles produce a clearer signature in the LHCb detector than neutral particles.

Requirements on the output of these BDT classifiers are optimised simultaneously by employing pseudoexperiments (see section 5). The pair of requirements that yields the minimum average uncertainty on R_K, accounting for the statistical and the dominant systematic contributions, across the pseudoexperiments is then used. The requirement on the combinatorial BDT output for the muon mode is determined by optimising the expected signal significance. For this calculation, the signal yield is estimated using measured

JHEP07(2025)198

values of the $B^+ \to K^+\mu^+\mu^-$ and $B^+ \to K^+ J/\psi(\to \mu^+\mu^-)$ branching fractions [60, 62]. The background yield is determined by extrapolating the combinatorial yield observed in the upper invariant-mass sideband into the region under the signal.

The B^+ candidates are required to have a three-body invariant mass, $m(K^+\ell^+\ell^-)$, around the known B^+ mass [60]. The invariant-mass ranges used for the electron and muon channels differ significantly due to their drastically different resolution. Candidates in the rare muon channel are required to have $5180 < m(K^+\mu^+\mu^-) < 5600\,\text{MeV}/c^2$, which is chosen to completely exclude partially reconstructed decays in the lower invariant-mass sideband. On the other hand, candidates in the rare electron channel are required to have $4300 < m(K^+e^+e^-) < 6300\,\text{MeV}/c^2$. The wider invariant-mass requirement improves the precision with which the rare electron yield can be determined, as discussed further in section 5.2.

The selection applied to the normalisation channels is identical to the rare channels, with the exception of the q^2 and $m(K^+\ell^+\ell^-)$ ranges. Due to the good q^2 resolution for muonic decays, the requirement of $8.68 < q^2 < 10.09\,\text{GeV}^2/c^4$ is applied to the $B^+ \to K^+ J/\psi(\to \mu^+\mu^-)$ mode. The q^2_{track} selection applied to the $B^+ \to K^+ J/\psi(\to e^+e^-)$ channel is chosen to be that which best aligns the $m(K^+e^+e^-)$ distribution between the resonant $B^+ \to K^+ J/\psi(\to e^+e^-)$ and nonresonant $B^+ \to K^+e^+e^-$ simulation. A selection of $7.1 < q^2_{\text{track}} < 10.0\,\text{GeV}^2/c^4$ is employed to ensure the maximal amount of kinematic overlap between the normalisation channel and the rare signal channel.

For the normalisation channels, improvement in the resolution of the three-body invariant mass can be achieved by constraining the invariant mass of the dilepton system to that of the relevant intermediate resonance. This is implemented via the *Decay Tree Fitter* [63] algorithms. The invariant-mass fit of the $B^+ \to K^+ J/\psi(\to \mu^+\mu^-)$ channel is performed in the range $5180 < m_{J/\psi}(K^+\mu^+\mu^-) < 5600\,\text{MeV}/c^2$ whereas the slightly wider range $5080 < m_{J/\psi}(K^+e^+e^-) < 5680\,\text{MeV}/c^2$ is used for the $B^+ \to K^+ J/\psi(\to e^+e^-)$ channel. The efficiency of the $m(K^+\ell^+\ell^-)$ selection requirement in all channels is above 99%. Therefore, any efficiency-related systematic uncertainty associated with differences in the invariant-mass selection applied to the normalisation and rare channels is negligible.

Finally, for events with more than one candidate after the full selection, the candidate with the highest combinatorial BDT response is retained. The fraction of rejected multiple candidates is at the subpercent level.

4 Efficiency correction and cross-checks

The efficiencies are computed from simulation that is corrected using data following the procedure described in refs. [64, 65]. Each correction is applied with respect to the preceding one. Firstly, the tracking efficiency for electrons is determined using a tag-and-probe method applied to a sample of $B^+ \to K^+ J/\psi(\to e^+e^-)$ decays [66]. The difference in tracking efficiency between data and simulated samples is corrected as a function of the pseudorapidity, the azimuthal angle ϕ and the p_{T} of the probe particle. The effect of these corrections is less than 1%, reflecting the good agreement between simulation and data. The efficiency of the PID requirements is obtained using data control channels that can be efficiently selected without the use of PID criteria [67].

JHEP07(2025)198

The samples include $D^{*+} \to D^0(\to K^-\pi^+)\pi^+$ decays for hadron (mis)identification, $B^+ \to K^+J/\psi(\to \mu^+\mu^-)$ decays for muon identification, and $B^+ \to K^+J/\psi(\to e^+e^-)$ decays for electron identification. For the muon and hadron calibration samples, background contributions are subtracted using the *sPlot* procedure [68, 69], and PID efficiencies are computed in bins of the probe's transverse momentum and pseudorapidity. The *sPlot* procedure is not applicable to the electron calibration sample due to correlations between the momentum of the probe electron and reconstructed B^+ mass, as the mass resolution is strongly affected by the electron energy loss before the calorimeter. Instead, the fraction of candidates passing the electron PID criteria is estimated by fitting the invariant-mass distribution of the $B^+ \to K^+J/\psi(\to e^+e^-)$ data twice: once with no PID selection applied and again with the electron PID selection applied to the probe. This is repeated in bins of the probe's transverse momentum, pseudorapidity, and whether or not bremsstrahlung is recovered for the probe.

The calibration of the PID efficiency implicitly assumes that the PID response of each final-state particle forming a B^+ candidate is independent of one another, with the exception of kinematic correlations. This assumption is tested using simulation samples and is found to have a negligible effect on the overall efficiency.

An initial set of corrections are derived to correct for the mismodelling of the B^+ production kinematics, impact parameter and vertex quality in the simulation. These corrections are obtained using the $B^+ \to K^+J/\psi(\to \mu^+\mu^-)$ channel and are applied to both muon and electron channels, after PID and tracking efficiencies have been corrected for. The corrections to the efficiencies discussed in the following are obtained on top of these initial corrections to the simulation.

The largest efficiency difference between muons and electrons originates from the trigger, where the E_{T} requirement for electrons is significantly more restrictive than the muon p_{T} requirement. The normalisation channels are employed to compare the trigger response between data and simulation using the tag-and-probe method. For example, using $B^+ \to K^+J/\psi(\to e^+e^-)$ decays, the tag kaon is required to pass a set of trigger requirements. The efficiency of the electron trigger is then determined by the fraction of candidates in which at least one of the two probe electrons passes the electron trigger requirements. This efficiency is compared between data and simulation as a function of the maximum E_{T} of the two electrons, which is expected to be the kinematic variable on which the electron trigger efficiency most strongly depends. The efficiency for the muon trigger is determined similarly, but as a function of the p_{T} of the muon.

An additional correction is obtained to reduce any residual mismodelling of the B^+ production kinematic and vertex-reconstruction quality. A gradient boosted reweighting procedure [70] is applied as a function of $p_{\mathrm{T}}(B^+)$, $\eta(B^+)$, $\chi^2_{\mathrm{DV}}(B^+)$ and $\chi^2_{\mathrm{IP}}(B^+)$ variables. The quantity $\chi^2_{\mathrm{DV}}(B^+)$ represents the fit quality of the B^+ decay vertex, whereas $\chi^2_{\mathrm{IP}}(B^+)$ is defined as the difference in the vertex-fit χ^2 of the PV when reconstructed with and without the B^+ candidate. These corrections are obtained using the $B^+ \to K^+J/\psi(\to \mu^+\mu^-)$ channel and are assumed to be independent of the lepton species. A comparison of the $B^+ \to K^+J/\psi(\to \mu^+\mu^-)$ data and simulation, both before and after the corrections, is presented in figure 3.

JHEP07(2025)198

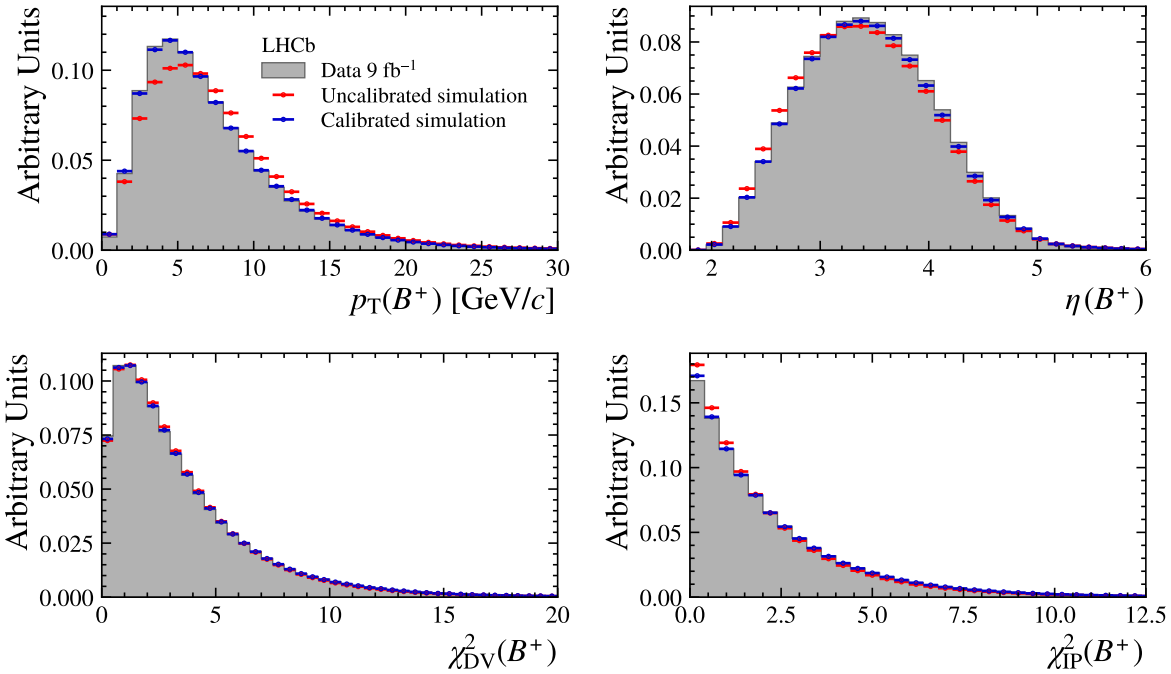

Figure 3. Distributions of reconstructed B^+ meson properties for (grey) $B^+ \to K^+ J/\psi(\to \mu^+\mu^-)$ data compared to simulation (red) before and (blue) after corrections are applied.

The quantity q^2_{track}, which is used to select both the electron normalisation and rare modes, is known to be incorrectly modelled in the simulation. For the normalisation modes' efficiencies, a correction is therefore derived using $B^+ \to K^+ J/\psi(\to e^+e^-)$ simulation and data samples. The invariant-mass distribution of the electron modes depends significantly on the outcome of the bremsstrahlung recovery algorithm. Therefore, the samples are split into the corresponding 0γ, 1γ, and 2γ categories, depending on whether photons are added to none, one, or both electron candidates. For each bremsstrahlung category the q^2_{track} distribution in simulation is fitted with a combination of Crystal Ball functions [71]. The resulting models are then convolved with a Gaussian function, and the corresponding $B^+ \to K^+ J/\psi(\to e^+e^-)$ data is fitted, with peak position and standard deviation determined from this fit. The extracted Gaussian function is then used to smear the q^2_{track} variable in the simulation, improving the agreement in resolution between the simulation and data.

The efficiencies computed using simulation are validated by measuring the branching fraction ratios of the resonant control modes, which have been shown to be consistent with LU [60]. The first of these is the single-ratio test, defined as:

$$\begin{aligned} r_{J/\psi} &\equiv \frac{\mathcal{B}(B^+ \to K^+ J/\psi(\to \mu^+\mu^-))}{\mathcal{B}(B^+ \to K^+ J/\psi(\to e^+e^-))} \\ &= \frac{N(B^+ \to K^+ J/\psi(\to \mu^+\mu^-))}{\varepsilon(B^+ \to K^+ J/\psi(\to \mu^+\mu^-))} \cdot \frac{\varepsilon(B^+ \to K^+ J/\psi(\to e^+e^-))}{N(B^+ \to K^+ J/\psi(\to e^+e^-))}. \end{aligned} \tag{4.1}$$

In this expression, $N(X)$ is the measured yield for decay X, while $\varepsilon(X)$ denotes the corresponding selection efficiency, which incorporates the effects of all the requirements outlined in section 3. The large branching fraction for $B^+ \to K^+ J/\psi(\to \ell^+\ell^-)$ decays means that

JHEP07(2025)198

$r_{J/\psi}$ is expected to have a small statistical uncertainty. Furthermore, since $r_{J/\psi}$ is a single-ratio, obtaining a result consistent with unity requires accurate control of the muon and electron efficiencies.

Additionally, the double-ratio between the $\psi(2S)$ and J/ψ control modes,

$$\begin{aligned} R_{\psi(2S)} &\equiv \frac{\mathcal{B}(B^+ \to K^+\psi(2S)(\to \mu^+\mu^-))}{\mathcal{B}(B^+ \to K^+\psi(2S)(\to e^+e^-))} \cdot \frac{\mathcal{B}(B^+ \to K^+J/\psi(\to e^+e^-))}{\mathcal{B}(B^+ \to K^+J/\psi(\to \mu^+\mu^-))} \\ &= \frac{N(B^+ \to K^+\psi(2S)(\to \mu^+\mu^-))}{\varepsilon(B^+ \to K^+\psi(2S)(\to \mu^+\mu^-))} \cdot \frac{\varepsilon(B^+ \to K^+\psi(2S)(\to e^+e^-))}{N(B^+ \to K^+\psi(2S)(\to e^+e^-))} \cdot \frac{1}{r_{J/\psi}}, \end{aligned} \tag{4.2}$$

is measured. Since $R_{\psi(2S)}$ is a double-ratio and both the $\psi(2S)$ and J/ψ control mode datasets are large, this measurement is statistically precise with a small efficiency-related systematic uncertainty. The sources of systematic uncertainty associated with the selection efficiencies appearing in eq. (4.1) and eq. (4.2) are presented in section 6. Resonant $B^+ \to K^+\psi(2S)(\to \mu^+\mu^-)$ candidates are required to have $12.5 < q^2 < 14.2\,\mathrm{GeV}^2/c^4$, whereas $B^+ \to K^+\psi(2S)(\to e^+e^-)$ candidates are selected with $10.5 < q^2_{\mathrm{track}} < 14.2\,\mathrm{GeV}^2/c^4$. The latter requirement significantly reduces backgrounds from $B^+ \to K^+J/\psi(\to e^+e^-)$ decays that would otherwise leak into the $B^+ \to K^+\psi(2S)(\to e^+e^-)$ data if q^2 is used. Resonant $B^+ \to K^+\psi(2S)(\to \ell^+\ell^-)$ candidates are selected with $5180 < m_{\psi(2S)}(K^+\ell^+\ell^-) < 5600\,\mathrm{MeV}/c^2$, where $m_{\psi(2S)}(K^+\ell^+\ell^-)$ is the reconstructed B^+ mass computed with the mass of the dilepton system constrained to the known $\psi(2S)$ mass [60].

The yields of the control modes are determined using extended unbinned maximum-likelihood fits to the dilepton-constrained invariant-mass distribution. A breakdown of the selection efficiencies and yields for the control channels is reported in table 1. The fit results are shown in figure 4. In the $m_{J/\psi}(K^+\mu^+\mu^-)$ and $m_{\psi(2S)}(K^+\mu^+\mu^-)$ invariant-mass distributions, the small disagreement near $5400\,\mathrm{MeV}/c^2$ has a negligible impact on the signal-yield determination. Moreover, contributions of misidentified $B^+ \to \pi^+\psi(2S)(\to e^+e^-)$ decays where the final-state pion is misidentified as a kaon, are found to be negligible in $B^+ \to K^+\psi(2S)(\to e^+e^-)$ decays. The resulting control mode yields are combined with efficiencies calculated using the corrected simulation and give

$$\begin{aligned} r_{J/\psi} &= 0.997 \pm 0.003 \pm 0.055, \\ R_{\psi(2S)} &= 1.002 \pm 0.009 \pm 0.004, \end{aligned}$$

where the first uncertainty is statistical and the second is systematic (see section 6). Both cross-checks are consistent with the SM expectation of unity.

The distributions of variables, such as the opening angle and minimum transverse momentum of the final-state leptons, are expected to depend strongly on q^2. Incorrectly modelling these distributions can result in biases in the efficiencies that do not cancel well in the double-ratio. Therefore, the single-ratio $r_{J/\psi}$ is measured in intervals of these variables (see figure 5); the absence of significant variations in the observed distributions demonstrates sufficient control of the efficiencies for an unbiased measurement of R_K. The uncertainties in figure 5 are statistical only, while efficiency-related systematic uncertainties (see section 6) are sufficient to explain the residual deviations from uniformity.

JHEP07(2025)198

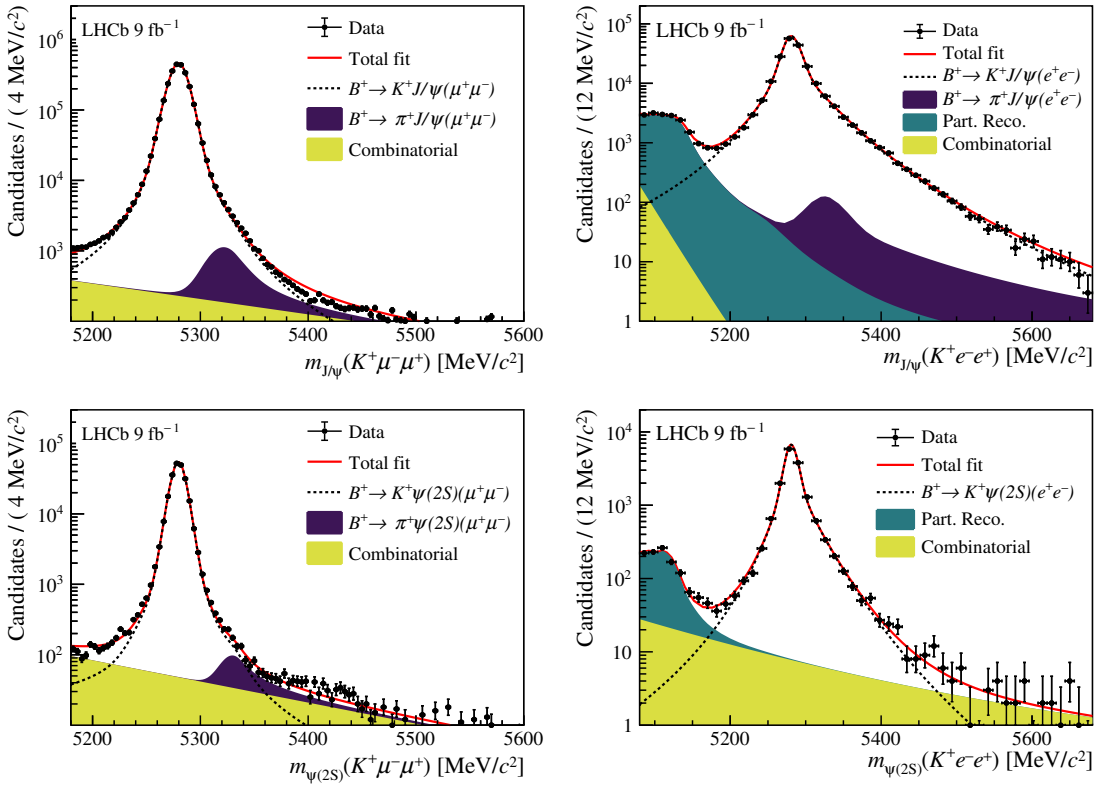

Figure 4. Distributions of (top) $m_{J/\psi}(K^+\ell^+\ell^-)$ of the $B^+\to K^+J/\psi(\to \ell^+\ell^-)$ channel and (bottom) $m_{\psi(2S)}(K^+\ell^+\ell^-)$ of the $B^+\to K^+\psi(2S)(\to \ell^+\ell^-)$ channel for the (left) muon and (right) electron modes, and corresponding fit results.

Decay mode	Yield	Efficiency (‰)
$B^+\to K^+J/\psi(\to e^+e^-)$	$203\,000 \pm 450$	1.388 ± 0.002
$B^+\to K^+J/\psi(\to \mu^+\mu^-)$	$2\,280\,000 \pm 1\,500$	15.680 ± 0.015
$B^+\to K^+\psi(2S)(\to e^+e^-)$	$15\,700 \pm 130$	1.325 ± 0.003
$B^+\to K^+\psi(2S)(\to \mu^+\mu^-)$	$201\,300 \pm 450$	17.051 ± 0.018

Table 1. Yields of the resonant channels obtained from the fits to the data and the corresponding efficiencies determined using calibrated simulation samples. The quoted uncertainties account for statistical effects only.

5 R_K measurement method

Similar to the formulation of $R_{\psi(2S)}$ in eq. (4.2), R_K can be measured using the double-ratio

$$R_K = \frac{N(B^+\to K^+\mu^+\mu^-)}{\varepsilon(B^+\to K^+\mu^+\mu^-)} \cdot \frac{\varepsilon(B^+\to K^+e^+e^-)}{N(B^+\to K^+e^+e^-)} \cdot \frac{1}{r_{J/\psi}}. \tag{5.1}$$

The terms $\varepsilon(B^+\to K^+e^+e^-)$ and $\varepsilon(B^+\to K^+\mu^+\mu^-)$ represent the selection efficiencies of rare $B^+\to K^+e^+e^-$ and $B^+\to K^+\mu^+\mu^-$ decays, respectively. These are model-dependent quantities as they are computed by integrating over a model of the q^2_{true} distribution of the

JHEP07(2025)198

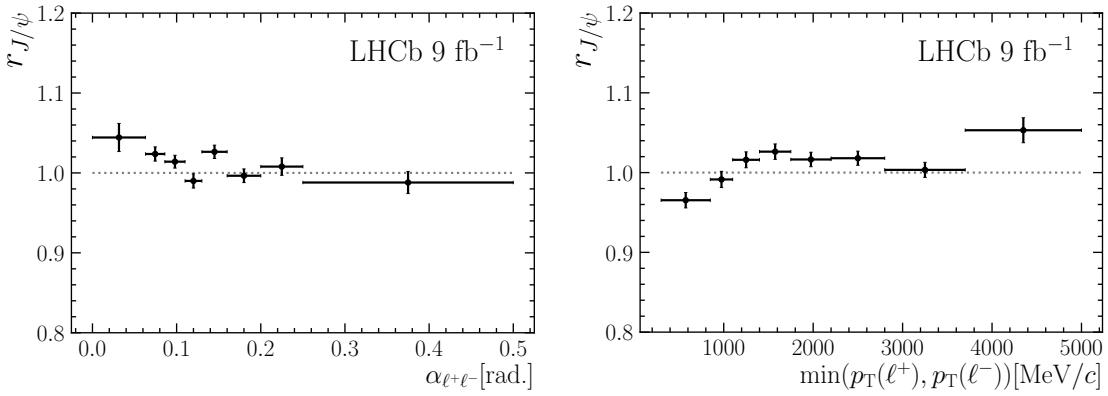

Figure 5. Value of $r_{J/\psi}$ as a function of (left) the opening angle between the leptons $\alpha_{\ell^+\ell^-}$ calculated in the laboratory frame, and (right) the minimum $p_{\rm T}$ of the leptons. The error bars shown are statistical only.

decay, where $q^2_{\rm true} \equiv (p_{B^+} - p_{K^+})^2$ is the squared momentum transferred to the dilepton pair. Here and in the following, the subscript *true* is used to indicate quantities prior to any final state radiation and detector resolution effects. This model dependence is problematic since multiple broad open-charm resonances exist in the high-q^2 region, as well as interference effects with the upper tail of the nearby large $\psi(2S)$ resonance, both of which are not precisely known.

To demonstrate the effect of a large mismodelling on the efficiencies, an example is considered using two significantly different $q^2_{\rm true}$ spectra. The baseline distribution of $q^2_{\rm true}$ is obtained from a measurement using $B^+ \to K^+\mu^+\mu^-$ decays [62], and is shown as the red histogram on the left-hand side of figure 6. In contrast, the blue histogram represents a simplified $q^2_{\rm true}$ model [72], which accounts only for penguin contributions to the decay amplitude. The ratio of rare-mode integrated selection efficiencies, $\varepsilon(B^+ \to K^+e^+e^-)/\varepsilon(B^+ \to K^+\mu^+\mu^-)$, is calculated using each model and illustrated by the horizontal lines on the right-hand side of figure 6. In this extreme example, the ratio shifts by approximately 5.5%, depending on the $q^2_{\rm true}$ model used, which would directly translate to a bias in R_K if measured using eq. (5.1). This motivates using a less model-dependent method for determining R_K. The method described in this paper reduces the uncertainty associated with altering the $q^2_{\rm true}$ model in this extreme example to at most 0.5%.

To reduce the $q^2_{\rm true}$ model dependence, one can exploit cancellations in the ratio of efficiencies in eq. (5.1). In the scenario that both the $q^2_{\rm true}$ spectra and the $q^2_{\rm true}$ dependence of the selection are identical between the muon and electron modes, any model dependence cancels in the ratio of efficiencies. In the case of LU, as in the SM, the $q^2_{\rm true}$ spectra of each mode are identical. However, the $q^2_{\rm true}$ dependence of the selection efficiencies of each mode is dramatically different, primarily due to the $q^2_{\rm track}$ requirement used to select $B^+ \to K^+e^+e^-$ decays. This can be circumvented by weighting the muon data as a function of q^2, such that the $q^2_{\rm true}$ dependence of the muon efficiency aligns with that of the electron mode. The weights applied to the rare muon data to achieve this alignment, $w_\varepsilon(q^2_{\rm true})$, are defined as the ratio of the muon and electron efficiencies as a function of $q^2_{\rm true}$ as shown on the right-hand side of figure 6. For each of the previously considered $q^2_{\rm true}$ models, the $w_\varepsilon(q^2_{\rm true})$ distribution changes

JHEP07(2025)198

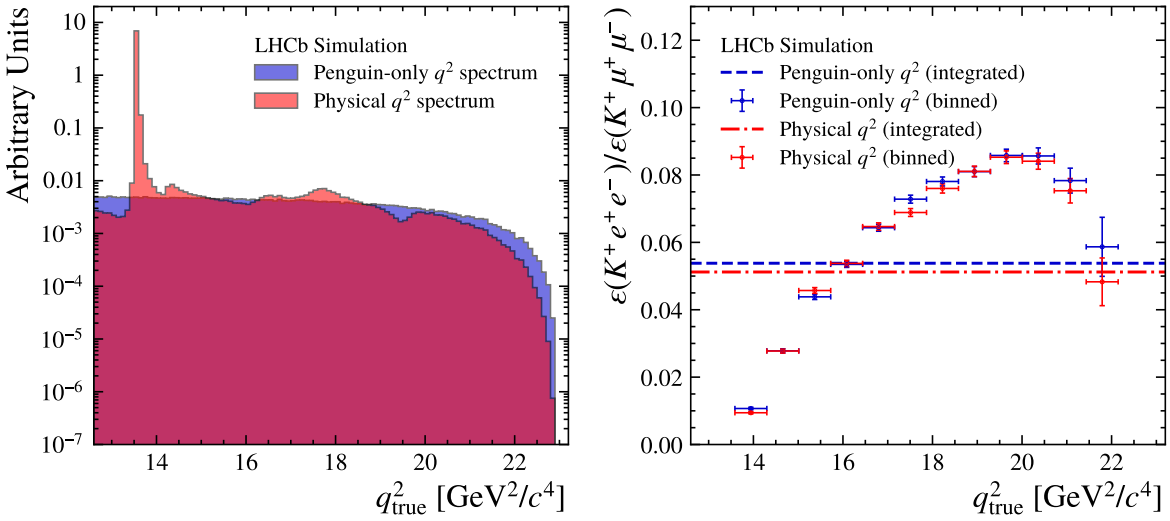

Figure 6. (left) Comparison of the q^2_{true} distribution and (right) the ratio of efficiencies between muonic and electronic rare mode decay channels for two different q^2_{true} models. The ratio of efficiencies is shown for both a binned and integrated calculation (dashed lines). The q^2_{true} model is varied from a simplistic description that considers only rare mode decays (blue) to a more sophisticated model that includes resonant processes and interference effects (red).

only by a small amount when the q^2_{true} model is varied significantly, with the residual variation attributed to the limited size of the simulation samples and the finite binning. Furthermore, there is residual model dependence arising from the assumption that, for $B^+ \to K^+\mu^+\mu^-$ decays, q^2 and q^2_{true} are equivalent. The impact of this assumption on R_K is minimal, and a more detailed discussion is presented in section 6.

Before applying the weights $w_\varepsilon(q^2_{\text{true}})$ to the rare muon data, backgrounds are subtracted using the *sPlot* technique [68]. The *sPlot* method is performed by fitting the $m(K^+\mu^+\mu^-)$ distribution of the rare muon data, as described in section 5.1. Each candidate in the rare muon data, indexed by i, is then represented by an *sWeight*, $s\mathcal{W}_i$. Using the *sWeights*, R_K is determined as

$$R_K = \underbrace{\frac{1}{r_{J/\psi}} \cdot \sum_i s\mathcal{W}_i \cdot w^i_\varepsilon(q^2_{\text{true}})}_{C} \cdot \frac{1}{N(B^+ \to K^+e^+e^-)}, \tag{5.2}$$

where the sum over i corresponds to the sum over fully selected candidates in the rare muon data. Importantly, unlike the fit strategy described in refs. [29, 30], R_K is not the result of a simultaneous fit to rare electron and rare muon data. Instead, R_K is extracted in the following manner: all efficiency terms, resonant channel yields, and information from the rare muon data are combined into the factor C, which corresponds to the expected yield of rare electron decays when $R_K = 1$. The yield of $B^+ \to K^+e^+e^-$ decays, denoted $N(B^+ \to K^+e^+e^-)$, is determined by performing an extended unbinned maximum-likelihood fit to the $m(K^+e^+e^-)$ distribution of the rare electron data, detailed in section 5.2. The likelihood function is parametrised in terms of C and R_K, allowing R_K to be determined directly from the fit. A Gaussian term is included in the likelihood function to constrain

JHEP07(2025)198

C to its estimated value, $C = 198.8 \pm 3.7\,(\text{stat}) \pm 2.2\,(\text{syst})$, as determined from data and simulation. This ensures that uncertainties related to efficiencies, resonant channel yields, and rare muon data are included in the uncertainty on R_K.

5.1 Muon rare mode fit

An extended unbinned maximum-likelihood fit is performed to the $m(K^+\mu^+\mu^-)$ distribution of the rare muon data as part of the *sPlot* procedure, used to derive *sWeights*. The fit model consists of three components: combinatorial background, $B^+ \to K^+\psi(2S)(\to \mu^+\mu^-)$ decays that leak up into the high-q^2 region due to resolution effects, and rare $B^+ \to K^+\mu^+\mu^-$ signal decays.

The signal peak model is derived in the following manner. For each data-taking year separately, the $m(K^+\mu^+\mu^-)$ distribution in the $B^+ \to K^+\mu^+\mu^-$ simulation is fitted with a sum of two Crystal Ball functions and a Gaussian distribution with a shared peak position but independent width parameters. The peak position and the global width of each distribution are corrected for data-simulation differences in the mass resolution, using a correction derived from the $B^+ \to K^+J/\psi(\to \mu^+\mu^-)$ resonant channel. The parameters from the fits to simulation are then fixed given their negligible uncertainties, and the distributions for each data-taking year are combined in a weighted sum.

The shape of the $B^+ \to K^+\psi(2S)(\to \mu^+\mu^-)$ background is modelled using the sum of a Crystal Ball function and a Gaussian distribution. The parameters of the model are determined from fitting the $B^+ \to K^+\psi(2S)(\to \mu^+\mu^-)$ simulation samples and then fixed in the fit to the data. The yield of the $B^+ \to K^+\psi(2S)(\to \mu^+\mu^-)$ component is constrained using a Gaussian penalty function to an estimate obtained by scaling the fitted $B^+ \to K^+\psi(2S)(\to \mu^+\mu^-)$ yield from the resonant mode fits (see figure 4) by the ratio of the rare and resonant q^2 selection efficiencies obtained from $B^+ \to K^+\psi(2S)(\to \mu^+\mu^-)$ simulation.

An exponential function is used to model the combinatorial background, with its normalisation and slope parameter allowed to float freely in the fit. The fit to the rare muon mode data is shown in figure 7. The fitted yield of $B^+ \to K^+\mu^+\mu^-$ decays is $N(B^+ \to K^+\mu^+\mu^-) = 4\,008 \pm 71$.

5.2 Electron rare mode fit

The yield of $B^+ \to K^+e^+e^-$ decays, $N(B^+ \to K^+e^+e^-)$, is extracted by performing an extended unbinned maximum-likelihood fit to the $m(K^+e^+e^-)$ distribution of the rare electron data. The modelling of each component contributing to the fit is discussed below.

5.2.1 Signal peak

The invariant-mass distribution of the electron rare mode has a significant dependence on the bremsstrahlung category, therefore, the samples are split according to bremsstrahlung category and each resulting distribution is described by a different shape. Category 0γ is modelled by a sum of two Crystal Ball functions, with opposite tails with respect to the peak. Two Gaussian distributions are also included, one to improve the modelling of the low-mass tail and the other to improve the modelling of the core of the distribution. Similarly, category 1γ is modelled by the sum of two Crystal Ball functions and a Gaussian distribution that

JHEP07(2025)198

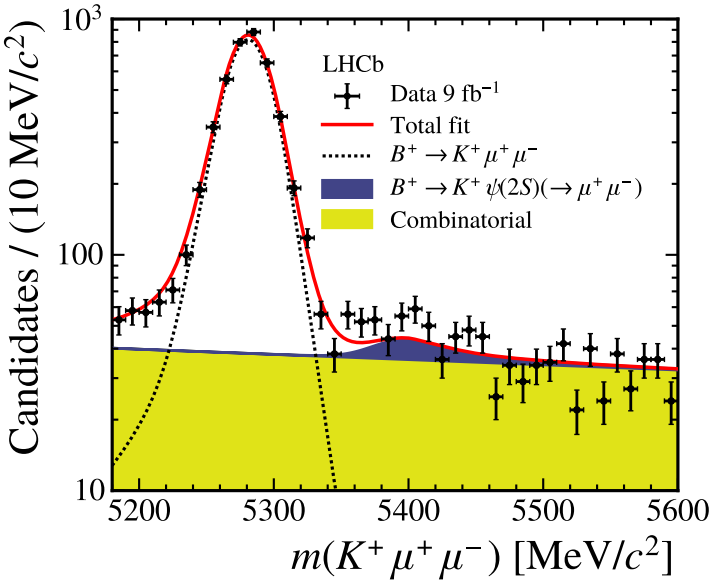

Figure 7. Distribution of $m(K^+\mu^+\mu^-)$ for the rare muon data compared to the result of the fit described in the text. The $B^+ \to K^+\psi(2S)(\to \mu^+\mu^-)$ background peaks at a shifted position with respect to the rare mode due to the q^2 requirement of being larger than the $\psi(2S)$ squared mass.

improves the modelling of the distribution's core. Finally, category 2γ is modelled with the sum of two Crystal Ball functions with tails on both sides of the peak. The shape parameters, initially obtained by fitting the simulated $m(K^+e^+e^-)$ distributions, are then corrected for data-simulation differences in resolution for each bremsstrahlung category. This procedure is analogous to the one adopted for the electron control modes (as described in section 4), however, due to the high-q^2 requirement on the electron rare mode, in this case the corrections are derived using simulation and data samples of $B^+ \to K^+\psi(2S)(\to e^+e^-)$ decays. The three smeared distributions are then summed with a fraction obtained from $B^+ \to K^+e^+e^-$ simulated events. Due to the use of q^2_{track} in the data selection, only a small fraction of decays are expected in 2γ (5.4%) compared to 0γ (54.7%) and 1γ (39.9%) categories. It is checked that the simulation accurately reproduces these fractions by comparing their values in data and simulated control modes. In the fit to the rare electron data, all the parameters associated with the description of the signal invariant-mass shape are fixed.

5.2.2 Partially reconstructed background

The most significant sources of partially reconstructed backgrounds are from B^+ and B^0 meson decays. The largest contributions are $B^0 \to K^*(892)^0(\to K^+\pi^-)e^+e^-$ and $B^+ \to K^*(892)^+(\to K^+\pi^0)e^+e^-$ decays, followed by much smaller contributions that involve other intermediate states. The simulation samples for $B^0 \to K^*(892)^0(\to K^+\pi^-)e^+e^-$ and $B^+ \to K^*(892)^+(\to K^+\pi^0)e^+e^-$ modes include $K\pi$ P-wave resonant decays only. Therefore, the $m(K\pi)$ spectrum for these samples is weighted to account for $K\pi$ S-wave contributions using the lineshape and the measured normalisation of ref. [73]. The simulation samples for each decay mode are combined into a single inclusive sample. Each process contributing to the inclusive sample is weighted to take into account its branching fraction and selection

JHEP07(2025)198

efficiency. The resulting inclusive sample is used to build a nonparametric Kernel Density Estimation (KDE), which is used as the model for the partially reconstructed background component in the rare electron mode fit. The shape is corrected for data-simulation differences in the $m(K^+e^+e^-)$ resolution in a similar manner as the signal decay. The yield of the partially reconstructed background component is allowed to float freely in the fit to the data. An additional partially reconstructed background, due to $B_s^0 \to \phi(\to K^+K^-)e^+e^-$ decays, is expected to make a small contribution of only five candidates [60]. This contribution is modelled similarly to the previous component; however, its yield is constrained in the fit.

5.2.3 Combinatorial background

The selection of candidates with large dilepton invariant mass enforces a lower bound on the possible value of $m(K^+e^+e^-)_{\text{true}}$, which significantly impacts the combinatorial background that would otherwise follow an exponential distribution. The effect of this restriction on the $m(K^+e^+e^-)_{\text{true}}$ distribution of the combinatorial background is modelled using the three-body phase-space function

$$\mathrm{d}\phi_3(x, m_K, q_{\text{true}}) = \kappa(x, m_K, q_{\text{true}})\,\mathrm{d}x\,\mathrm{d}q_{\text{true}}, \tag{5.3}$$

where $\kappa(x, m_K, q_{\text{true}})$ is the triangle function

$$\kappa(x, m_K, q_{\text{true}}) = \frac{\sqrt{x^2 - (m_K + q_{\text{true}})^2}}{x}\,\frac{\sqrt{x^2 - (m_K - q_{\text{true}})^2}}{x}, \tag{5.4}$$

which depends on the kaon mass, m_K, the invariant mass squared of the dilepton pair, q_{true}, and the three-body invariant mass $x \equiv m(K^+e^+e^-)_{\text{true}}$. The two-body term $\mathrm{d}\phi_2(q_{\text{true}}; p_{\ell^+}, p_{\ell^-})$ is neglected, since at high-dilepton invariant mass it is very close to one. The reconstructed mass distribution describing the combinatorial component at high-dilepton invariant mass is obtained by making the ansatz

$$\frac{\mathrm{d}\Gamma}{\mathrm{d}x}(x, q^{\text{min}}_{\text{true}}, q^{\text{max}}_{\text{true}}, \lambda) = \frac{1}{4x} e^{-\lambda x} \int_{q^{\text{min}}_{\text{true}}}^{q^{\text{max}}_{\text{true}}} \kappa(x, m_K, q_{\text{true}})\,\mathrm{d}q_{\text{true}} \tag{5.5}$$

where $q^{\text{min}}_{\text{true}}$ and $q^{\text{max}}_{\text{true}}$ are the kinematic boundaries of the measurement, and λ is the exponential slope. This model is hereafter referred to as the phase-space model.

The integrand of eq. (5.5) parametrised in terms of q^2_{true} and $m(K^+e^+e^-)_{\text{true}}$ is illustrated on the left-hand side of figure 8. Two different q^2_{true} regions are highlighted: one corresponding to the region $1.1 < q^2_{\text{true}} < 6.0\,\text{GeV}^2/c^4$, where the combinatorial background is expected to follow an exponential distribution, and the other corresponding to the high-q^2_{true} region probed by this analysis. The phase-space model for each q^2_{true} region is illustrated on the right-hand side of figure 8. The phase-space model for the region $1.1 < q^2_{\text{true}} < 6.0\,\text{GeV}^2/c^4$ is compatible with an exponential distribution with the same value of the slope parameter λ. Conversely, the phase-space model for the high-q^2_{true} region has the expected characteristic of decreasing in size as $m(K^+e^+e^-)_{\text{true}}$ decreases towards $4300\,\text{MeV}/c^2$.

The advantage of using a physics-motivated model to describe the combinatorial background lies in its ability to reduce the number of free parameters required to parametrise the shape. By fixing the parameters $q^{\text{min}}_{\text{true}}$ and $q^{\text{max}}_{\text{true}}$ to their expected values and only allowing

JHEP07(2025)198

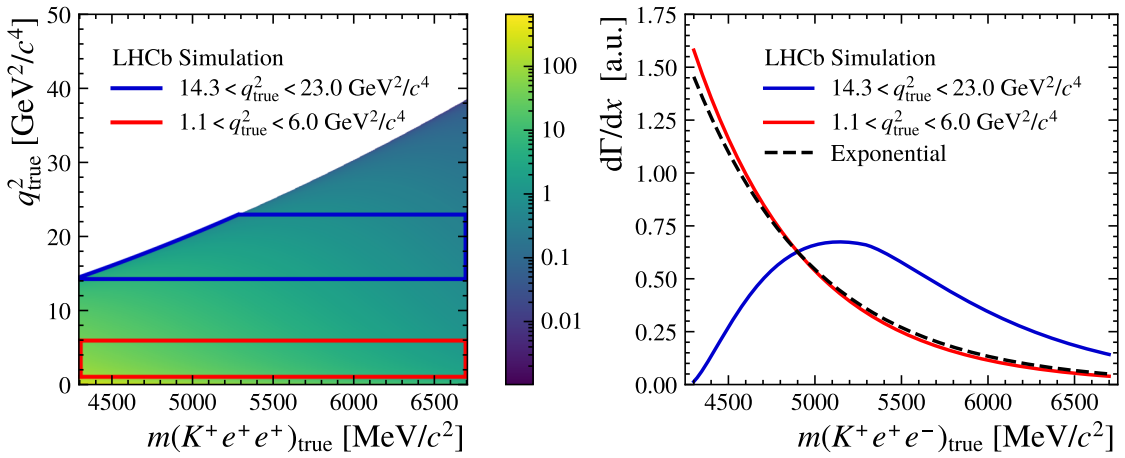

Figure 8. Visualisation of the phase space (left) in a two-dimensional representation of the integrand of eq. (5.5) parametrised in q^2_{true} and $m(K^+e^+e^-)_{\text{true}}$ and (right) the phase-space model for two highlighted q^2_{true} regions.

λ to freely float, the uncertainty on the extracted $B^+ \to K^+e^+e^-$ yield is reduced, which translates to a reduced R_K uncertainty.

The $m(K^+e^+e^-)_{\text{true}}$ distribution of combinatorial candidates in data is impacted by detector effects, which are not accounted for in the derivation of the phase-space model. To account for this, the phase-space model is corrected using data control samples.

The first control sample used is the mixed sample, which is obtained by combining a K^+, e^+ and e^- candidate from three randomly selected events from the data. For each new $K^+e^+e^-$ candidate, kinematic quantities such as $m(K^+e^+e^-)$, q^2_{track} and $m(K^+e^-)$ are computed. The mixed sample is used to derive corrections to the phase-space model to account for the sculpting from the charm-cascade kinematic veto $m(K^+e^-) > 1885\,\text{MeV}/c^2$, and the assumption in the derivation of the phase-space model that a cut is made on q^2_{true}, whereas in reality, the selection is based on q^2_{track}. Both effects act to exaggerate the sculpting, removing more candidates with a low value of $m(K^+e^+e^-)$.

The model is then compared to the rare electron mode data sample with an inverted selection requirement on the combinatorial BDT response. The inverted BDT requirement ensures that the sample is enriched in combinatorial background and that signal-like backgrounds are suppressed to negligible levels. The combinatorial model is fit to the inverted BDT sample, with only the λ parameter allowed to float. The fit result is illustrated by the red curve on the left-hand side of figure 9. The minor discrepancies between the inverted BDT data and the fitted model are a result of mismodelling effect of the selection requirements on the ansatz of eq. (5.5). To account for this, the combinatorial model is multiplied by a polynomial function that reduces these dependencies, demonstrated by the blue curve.

Finally, the BDT requirements have the effect of removing more candidates at higher values of $m(K^+e^+e^-)$, and shifting the peak of the combinatorial distribution towards lower values of $m(K^+e^+e^-)$. The $m(K^+e^+e^-)$ distribution is corrected to account for this warping using a dedicated $B^+ \to K^+e^+\mu^-$ control sample. This sample is expected to be dominated

JHEP07(2025)198

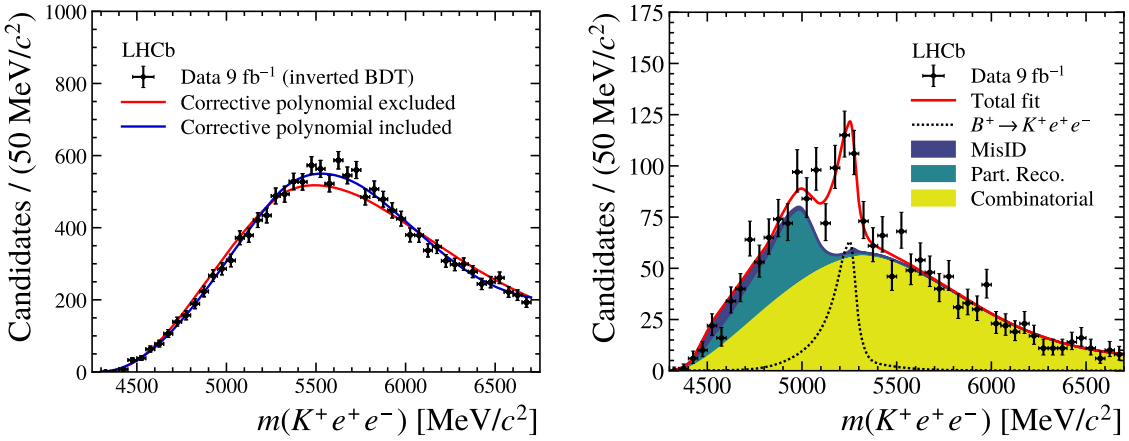

Figure 9. Fit projections comparing the combinatorial model to the rare electron mode data with (left) an inverted and (right) a loose cut on the combinatorial BDT output.

by combinatorial background, as $B^+ \to K^+e^+\mu^-$ decays are forbidden in the SM [74]. The selection applied to the $B^+ \to K^+e^+\mu^-$ data is aligned as much as possible to that applied to the $B^+ \to K^+e^+e^-$ data, with the exception of the PID requirements applied to select a muon in the final state. Using this sample, the mass-dependent efficiency of the BDT selection is determined and incorporated into the total combinatorial model.

To validate the BDT correction derived from the $B^+ \to K^+e^+\mu^-$ sample, a fit is performed to the electron rare mode data but with two modifications relative to the baseline fit used to determine R_K. First, all parameters associated with the shape of the combinatorial model are fixed to values obtained from the control samples. This differs from the baseline fit where the slope parameter λ is allowed to vary freely. Second, the data is selected with a cut on the output of the combinatorial BDT that is looser than the one used in the baseline determination of R_K, resulting in a sample that is enriched in combinatorial background. However, the BDT requirement remains sufficiently tight that it still significantly impacts the $m(K^+e^+e^-)$ distribution of the combinatorial background, the effect of which is re-evaluated using the $B^+ \to K^+e^+\mu^-$ sample. The result of the fit is presented on the right-hand side of figure 9. Despite the simplicity of the combinatorial model, good agreement is observed between the model and data, providing confidence that all relevant effects impacting the combinatorial background are well under control.

5.2.4 Misidentified background

Although PID selection requirements drastically suppress contributions from processes where a hadron is misidentified as an electron, it is necessary to estimate the size and shape of any residual misidentified background contributions, which fall into three main categories. The first two categories correspond to the fully reconstructed decays $B^+ \to K^+\pi^+\pi^-$ and $B^+ \to K^+K^+K^-$. In the former decay, the two pions are misidentified as electrons, whereas in the latter, two kaons are misidentified as electrons. Accurately modelling these backgrounds is of particular importance since they both peak close to the B^+ mass. Hence, incorrectly modelling these backgrounds can significantly bias the extracted $B^+ \to K^+e^+e^-$ yield and,

JHEP07(2025)198

Background	Data-based Yield	Simulation Yield
$B^+ \to K^+\pi^+\pi^-$	2.2 ± 0.9	1.24 ± 0.09
$B^+ \to K^+K^+K^-$	0.2 ± 0.4	0.90 ± 0.04
Part. reco. misID	14 ± 4	–

Table 2. Estimated yield of the misidentified backgrounds computed using the baseline method based on data, and alternatively computed using selection efficiencies derived from simulation samples and branching fractions from ref. [60].

consequently, R_K. The invariant-mass parametrisations of these two components are modelled with KDEs obtained using dedicated simulation samples.

A third contribution arises from partially reconstructed misidentified backgrounds, which include any process with one or two hadrons misidentified as an electron and a particle that is not reconstructed as part of the $K^+e^+e^-$ final state. Due to the missing energy taken by the unreconstructed particle, candidates in this category are expected to form a broad peak at low values of $m(K^+e^+e^-)$ compared to the B^+ mass. As there are many decays that contribute to this third category, most with imprecisely known branching fractions, it is impractical to model this background using simulated samples. Instead, an approach using data is utilised [29]. An orthogonal control sample that is enriched in misidentified background is constructed by inverting the electron PID requirements and leaving all other criteria unchanged. Weights derived from standard PID calibration samples are used to scale and reshape the inverted PID data. A fit to the weighted data with inverted PID requirements enables an estimate of the misidentified background to be determined whilst removing contributions from combinatorial candidates and signal decays that leak into the inverted PID region. In this fit, KDEs built using dedicated simulation samples represent the $B^+ \to K^+\pi^+\pi^-$ and $B^+ \to K^+K^+K^-$ backgrounds along with a phase-space distribution with $q^2_{\rm min}$ and λ parameters floating to describe the nonpeaking misidentified background. Systematic uncertainties relating to this approach are assessed in section 6, including one accounting for the fit model choice. The fit result is shown on the left-hand side of figure 10.

In the fit to the rare electron mode data, shown on the right-hand side of figure 10, the shape and normalisation parameters of the misidentified background component are fixed. The estimated yields of each misidentified background, obtained using the data-based approach, are presented in table 2. These are compared to alternative estimates derived using selection efficiencies computed from simulated samples reweighted to the measured Dalitz distribution and the measured branching fractions of $B^+ \to K^+\pi^+\pi^-$ and $B^+ \to K^+K^+K^-$ decays [60]. The uncertainty on the simulation-based estimates is primarily dominated by the precision of the $B^+ \to K^+\pi^+\pi^-$ and $B^+ \to K^+K^+K^-$ branching fractions and does not account for uncertainties related to the Dalitz distribution, which are expected to be significant. Despite this, the estimates based on simulation and data are consistent, providing confidence in the modelling of the misidentified background.

An additional cross-check is performed by measuring R_K under varying PID criteria, re-evaluating the misidentified background contribution at each step. A significant depen-

JHEP07(2025)198

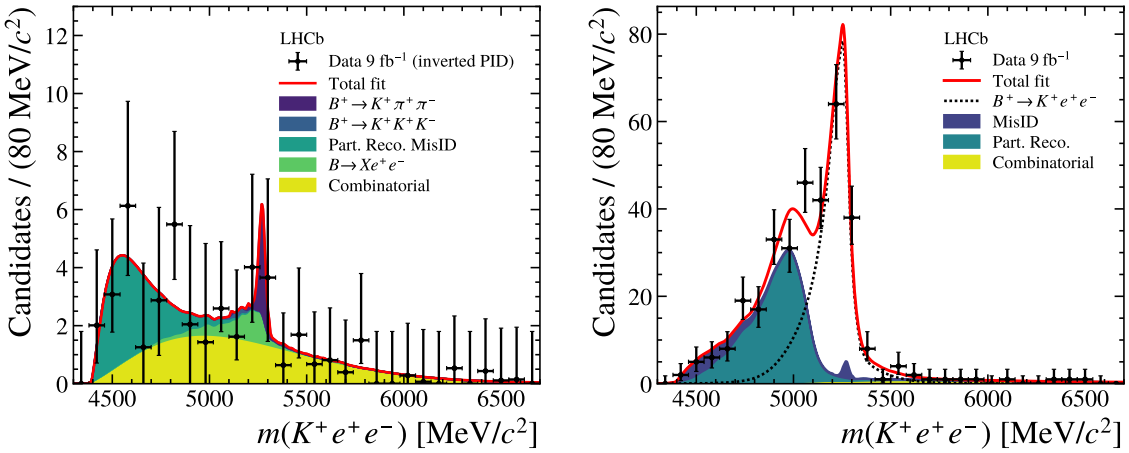

Figure 10. Invariant-mass distribution (left) of the inverted PID data control sample and (right) of the rare electron mode data, compared to the corresponding fits described in the text.

dence of R_K on the PID requirements could indicate shortcomings in the modelling of the misidentified background contribution. To assess this, the observed PID scan is compared to pseudoexperiments generated under the null hypothesis, assuming no such dependence. No trend is observed in the pseudoexperiments, and a p-value of 0.80 is obtained from the comparison. This result indicates good agreement between data and expectation, providing confidence in the robustness of the modelling of the misidentified background component.

5.2.5 Fit validation

The yield of $B^+ \to K^+e^+e^-$ decays, as determined from the fit to the rare electron data, is $N(B^+ \to K^+e^+e^-) = 182^{+17}_{-16}$ where the uncertainty is statistical only. The stability of the fit is evaluated using pseudoexperiments generated from the baseline fit result shown by the red line on the right side of figure 10. All pseudoexperiments consistently converge to a well-defined global minimum of the likelihood function, irrespective of the initial conditions of the fit.

6 Systematic uncertainties

The most significant sources of systematic uncertainty stem from the modelling of the invariant-mass fit to rare electron data. Additionally, there are systematic uncertainties relating to the correction chain applied to the simulated samples. Finally, there is a small source of systematic uncertainty arising from variations to the q^2_{true} model-independent approach for extracting R_K. All systematic uncertainties are expressed as percentages relative to the central fitted value of R_K. A summary of the systematic uncertainties affecting R_K is presented in table 3.

A large ensemble of pseudoexperiments generated from the baseline fit result are used to estimate the intrinsic bias on R_K, which is determined to be 1.1%. The bias is corrected in the final R_K result and is further included as a systematic uncertainty. Additional systematic uncertainties related to the modelling of components contributing to the invariant-mass spectrum are evaluated by fitting each pseudoexperiment twice: once with the *baseline* model and once with an *alternative* model. The R_K residuals, $\Delta R_K = R_K^{\text{alternative}} - R_K^{\text{baseline}}$, are then

JHEP07(2025)198

Source	$\sigma_{R_K}(\%)$
Fit bias	1.1
Signal model	0.9
Partially reconstructed background	2.2
Combinatorial background	1.2
Misidentified background	2.0
Excluded backgrounds	0.6
q^2_{true} model-independent method	0.6
Efficiency corrections	0.9

Table 3. Summary of relative systematic uncertainties on R_K, as described in the text.

calculated for the ensemble of pseudoexperiments. For each source of uncertainty, the largest of the mean or standard deviation of the distribution of residuals is used as the systematic uncertainty. In cases where there are multiple sources of systematic uncertainty associated with a single fit component, the figures in table 3 represent the sum in quadrature of all sources.

Model choices related to the signal peak in the fit to the rare electron data result in a 0.9% systematic uncertainty on R_K, which accounts for the following variations. Firstly the effect of varying the signal peak parametrisation is evaluated by instead using a KDE constructed using the $B^+ \to K^+e^+e^-$ simulation. Secondly, the uncertainty associated with the data-based correction to the $m(K^+e^+e^-)$ resolution of the signal peak is evaluated by using a signal peak excluding this correction. Finally, uncertainty associated with the limited size of the simulation sample used to derive the signal peak is evaluated by bootstrapping [75] the simulation samples for each pseudoexperiment and building a fresh KDE for each fit.

Systematic uncertainties related to the modelling of the partially reconstructed background component have a combined size of 2.2%. Similarly to the signal peak, the systematic uncertainty associated with the partially reconstructed background component includes the effects associated with the limited size of the simulation sample and neglecting the data-based $m(K^+e^+e^-)$ resolution correction. Two further sources of uncertainty are considered. First, rather than using the inclusive sample as discussed in section 5.2, an alternative parametrisation is derived using only the $B^+ \to K^{*+}(\to K^+\pi^0)e^+e^-$ simulation sample. Second, to account for any uncertainty associated with the weighting of the $B^0 \to K^{*0}(\to K^+\pi^-)e^+e^-$ and $B^+ \to K^{*+}(\to K^+\pi^0)e^+e^-$ simulation samples to include a $K\pi$ S-wave contribution, an alternative model is obtained with this contribution doubled.

Two variations of the combinatorial model are considered, with a combined systematic uncertainty of 1.2%. As outlined in section 5.2, a correction using data to the combinatorial model is included by multiplying the phase-space model by a polynomial function. For the baseline model, the parameters of the polynomial function are determined by fitting the inverted BDT data, as shown on the left-hand side of figure 9. The effect of using an alternative version of this correction is evaluated by determining its parameters by instead fitting the $B^+ \to K^+e^+\mu^-$ data. The combinatorial model additionally includes a correction that accounts for the effects of the BDT requirements. This correction is derived using the

JHEP07(2025)198

$B^+ \to K^+ e^+ \mu^-$ sample, where the primary source of uncertainty stems from the limited size of the $B^+ \to K^+ e^+ \mu^-$ sample. To address this, for each pseudoexperiment, an alternative combinatorial model is used that includes a BDT correction with parameters determined by fitting a bootstrapped version of the $B^+ \to K^+ e^+ \mu^-$ sample.

There are multiple sources of systematic uncertainty related to the misidentified background component, amounting to a combined uncertainty of 2.0%. The first source of systematic uncertainty is associated with the choice to fix the parameters of the misidentified background model when fitting the rare electron data. This approach ignores significant uncertainties related to the model parameters, stemming primarily from the small size of the control samples utilised for their estimation. To address this, the parameters of the misidentified background are fluctuated for each determination of $R_K^{\text{alternative}}$. The fluctuated parameter values are obtained by bootstrapping the control samples and repeating the data-based estimation method. A second source of systematic uncertainty involves varying the choice of model used to describe the misidentified background. As a variation to the baseline misidentified background model presented in section 5.2, a single KDE constructed using the weighted inverted PID data is used instead. Additional systematic uncertainties associated with the misidentified background component are evaluated by modifying elements of data control samples, such as changing the inverted PID requirements.

Two systematic uncertainties are evaluated to account for the effects of backgrounds with yields considered too small to include in the baseline fit. One uncertainty pertains to backgrounds that include a D meson, while the other relates to backgrounds that include a $\psi(2S)$ resonance. Together, these uncertainties have a combined size of 0.6%. Each systematic uncertainty is evaluated by fitting pseudoexperiments twice: first, using the baseline model, and second, by additionally injecting a background component. Each background is modelled with a KDE derived using simulation samples. The yield of each background component is fixed using selection efficiencies from simulation and branching fractions from ref. [60].

The newly adapted R_K extraction method significantly reduces any q^2_{true} model-dependence of this analysis. However, there remains a residual level of q^2_{true} model-dependence for the reasons discussed in section 5.2. Consequently, three sources of systematic uncertainty associated with the q^2_{true} model-independent extraction method are evaluated, which together contribute a total uncertainty of 0.6%. Each source of systematic uncertainty is evaluated by varying an aspect of the approach and assessing the percentage shift in the parameter C, which by virtue of eq. (5.2), translates to an equivalent shift in R_K. The q^2_{true} model-independent approach implicitly assumes $q^2_{\text{true}} \equiv q^2$ for muons. However, this assumption is not exact, so the effect of degrading the q^2 resolution in the muon mode samples is evaluated. The effect of explicitly varying the q^2_{true} model of simulated events is also evaluated. The baseline approach for computing C uses simulated samples generated with a q^2_{true} model that incorporates resonances and interference effects. As a variation, the simplified q^2_{true} model, including only penguin contributions, is used. The final source of systematic uncertainty is associated with the binning of the $w_\varepsilon(q^2_{\text{true}})$ weights, which is assessed by increasing the number of bins from the baseline value of 60 to 140.

JHEP07(2025)198

Differences between the rare and resonant modes and imperfections in the applied corrections result in residual uncertainties related to the efficiencies. These uncertainties are computed by measuring shifts in R_K when alternative corrections are applied to the simulation. The total efficiency-related systematic uncertainty on R_K, including all contributions outlined in the following text, is 0.9%. In the baseline approach, the $B^+ \to K^+ J/\psi(\to \mu^+\mu^-)$ data is used to derive corrections to the B^+ kinematic properties in the simulation thanks to the abundance and good resolution of that channel. Alternative corrections are derived by changing the variables corrected in the simulation and by using the $B^+ \to K^+ J/\psi(\to e^+e^-)$ data. Variations to the trigger corrections are also considered. Any potential bias introduced by the choice of tag is covered by deriving an alternative set of corrections, where the electron trigger response is computed on candidates that were instead triggered by the kaon candidate in the $B^+ \to K^+ J/\psi(\to e^+e^-)$ final state. Similar variations are studied by changing the trigger requirement applied to the control samples used to derive the PID corrections and by varying the kinematic binning used to obtain them. The systematic uncertainty associated with the mismodelling of particle multiplicity in simulation is determined by comparing the effect of adding to the initial sets of corrections three different multiplicity proxies. Finally, the impact of the data-simulation corrections to the q^2_{track} resolution is covered by computing the variation in R_K when the correction is not applied. This systematic uncertainty is significantly reduced by the choice to select the $B^+ \to K^+ J/\psi(\to e^+e^-)$ mode with a q^2_{track} selection.

7 Results and conclusions

The measured value for R_K at high-q^2, corrected for bias intrinsic to the rare electron mode fit, is

$$R_K(q^2 > 14.3\,\text{GeV}^2/c^4) = 1.08^{+0.11\,+0.04}_{-0.09\,-0.04}\,,$$

where the first uncertainty is statistical and the second is systematic. The data used for the measurement consists of beauty-meson decays produced in proton-proton collisions, corresponding to an integrated luminosity of $9\,\text{fb}^{-1}$, collected by the LHCb experiment between 2011 and 2018. Due to the limited sample size of the rare electron mode data, the statistical uncertainty of R_K is not Gaussian. Therefore, the confidence intervals of R_K are obtained through the likelihood profile shown in figure 11.

To determine separate statistical and systematic uncertainties, the likelihood profile is repeated twice, once excluding the contribution from systematic effects in the likelihood function and again including them. The former profile returns the statistical uncertainty, whereas the latter profile yields the total uncertainty on R_K. The systematic uncertainty is then determined by subtracting the statistical from the total uncertainty in quadrature.

This is the first measurement of R_K in the high-q^2 region at a hadron collider and the result is compatible with the SM and with previous measurements [26]. The measurement has complementary dependence on both background and efficiency mismodelling to measurements below the $\psi(2S)$ resonance [29, 30] and is the most precise measurement of LU in the kinematic region above the $\psi(2S)$ resonance [26, 31].

JHEP07(2025)198

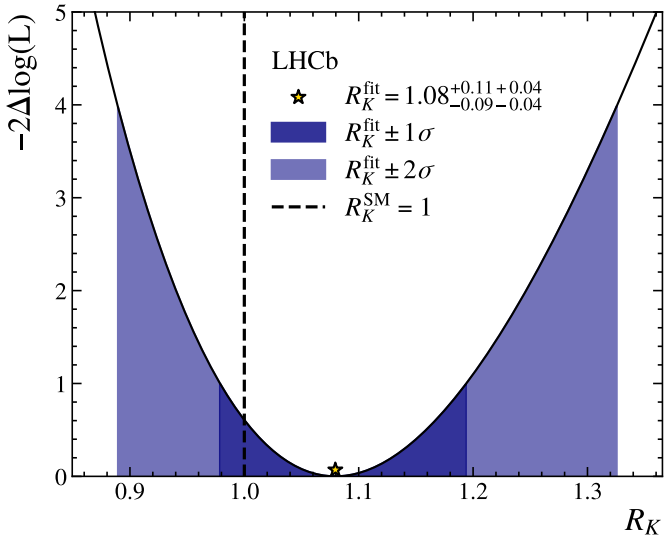

Figure 11. Likelihood (L) scan for R_K with the best-fit value (golden star) and expected SM value (vertical dashed line) highlighted. The 1σ and 2σ confidence regions are indicated by the dark and light-shaded regions, respectively.

Acknowledgments

We express our gratitude to our colleagues in the CERN accelerator departments for the excellent performance of the LHC. We thank the technical and administrative staff at the LHCb institutes. We acknowledge support from CERN and from the national agencies: ARC (Australia); CAPES, CNPq, FAPERJ and FINEP (Brazil); MOST and NSFC (China); CNRS/IN2P3 (France); BMBF, DFG and MPG (Germany); INFN (Italy); NWO (Netherlands); MNiSW and NCN (Poland); MCID/IFA (Romania); MICIU and AEI (Spain); SNSF and SER (Switzerland); NASU (Ukraine); STFC (United Kingdom); DOE NP and NSF (U.S.A.). We acknowledge the computing resources that are provided by ARDC (Australia), CBPF (Brazil), CERN, IHEP and LZU (China), IN2P3 (France), KIT and DESY (Germany), INFN (Italy), SURF (Netherlands), Polish WLCG (Poland), IFIN-HH (Romania), PIC (Spain), CSCS (Switzerland), and GridPP (United Kingdom). We are indebted to the communities behind the multiple open-source software packages on which we depend. Individual groups or members have received support from Key Research Program of Frontier Sciences of CAS, CAS PIFI, CAS CCEPP, Fundamental Research Funds for the Central Universities, and Sci. & Tech. Program of Guangzhou (China); Minciencias (Colombia); EPLANET, Marie Skłodowska-Curie Actions, ERC and NextGenerationEU (European Union); A*MIDEX, ANR, IPhU and Labex P2IO, and Région Auvergne-Rhône-Alpes (France); Alexander-von-Humboldt Foundation (Germany); ICSC (Italy); Severo Ochoa and María de Maeztu Units of Excellence, GVA, XuntaGal, GENCAT, InTalent-Inditex and Prog. Atracción Talento CM (Spain); SRC (Sweden); the Leverhulme Trust, the Royal Society and UKRI (United Kingdom).

JHEP07(2025)198

Data Availability Statement. This article has data included as electronic supplementary material.

Code Availability Statement. This article has associated code in a code repository.

Open Access. This article is distributed under the terms of the Creative Commons Attribution License (CC-BY4.0), which permits any use, distribution and reproduction in any medium, provided the original author(s) and source are credited.

References

[1] A. Celis, J. Fuentes-Martín, M. Jung and H. Serodio, *Family nonuniversal Z' models with protected flavor-changing interactions*, *Phys. Rev. D* **92** (2015) 015007 [arXiv:1505.03079] [INSPIRE].

[2] A. Falkowski, M. Nardecchia and R. Ziegler, *Lepton flavor non-universality in B-meson decays from a U(2) flavor model*, *JHEP* **11** (2015) 173 [arXiv:1509.01249] [INSPIRE].

[3] A. Crivellin, G. D'Ambrosio and J. Heeck, *Explaining $h \to \mu^{\pm}\tau^{\mp}$, $B \to K^*\mu^+\mu^-$ and $B \to K\mu^+\mu^-/B \to Ke^+e^-$ in a two-Higgs-doublet model with gauged $L_\mu - L_\tau$*, *Phys. Rev. Lett.* **114** (2015) 151801 [arXiv:1501.00993] [INSPIRE].

[4] R. Barbieri, C.W. Murphy and F. Senia, *B-decay anomalies in a composite leptoquark model*, *Eur. Phys. J. C* **77** (2017) 8 [arXiv:1611.04930] [INSPIRE].

[5] D. Buttazzo, A. Greljo, G. Isidori and D. Marzocca, *B-physics anomalies: a guide to combined explanations*, *JHEP* **11** (2017) 044 [arXiv:1706.07808] [INSPIRE].

[6] LHCb collaboration, *Comprehensive analysis of local and nonlocal amplitudes in the $B^0 \to K^{*0}\mu^+\mu^-$ decay*, *JHEP* **09** (2024) 026 [arXiv:2405.17347] [INSPIRE].

[7] LHCb collaboration, *Amplitude analysis of the $B^0 \to K^{*0}\mu^+\mu^-$ decay*, *Phys. Rev. Lett.* **132** (2024) 131801 [arXiv:2312.09115] [INSPIRE].

[8] LHCb collaboration, *Determination of short- and long-distance contributions in $B^0 \to K^{*0}\mu^+\mu^-$ decays*, *Phys. Rev. D* **109** (2024) 052009 [arXiv:2312.09102] [INSPIRE].

[9] LHCb collaboration, *Angular analysis of the rare decay $B_s^0 \to \phi\mu^+\mu^-$*, *JHEP* **11** (2021) 043 [arXiv:2107.13428] [INSPIRE].

[10] LHCb collaboration, *Branching fraction measurements of the rare $B_s^0 \to \phi\mu^+\mu^-$ and $B_s^0 \to f_2'(1525)\mu^+\mu^-$ decays*, *Phys. Rev. Lett.* **127** (2021) 151801 [arXiv:2105.14007] [INSPIRE].

[11] CMS collaboration, *Angular analysis of the $B^0 \to K^*(892)^0\mu^+\mu^-$ decay in proton-proton collisions at $\sqrt{s} = 13$ TeV*, *Phys. Lett. B* **864** (2025) 139406 [arXiv:2411.11820] [INSPIRE].

[12] A. Bharucha, D.M. Straub and R. Zwicky, *$B \to V\ell^+\ell^-$ in the Standard Model from light-cone sum rules*, *JHEP* **08** (2016) 098 [arXiv:1503.05534] [INSPIRE].

[13] R.R. Horgan, Z. Liu, S. Meinel and M. Wingate, *Lattice QCD calculation of form factors describing the rare decays $B \to K^*\ell^+\ell^-$ and $B_s \to \phi\ell^+\ell^-$*, *Phys. Rev. D* **89** (2014) 094501 [arXiv:1310.3722] [INSPIRE].

[14] N. Gubernari, D. van Dyk and J. Virto, *Non-local matrix elements in $B_{(s)} \to \{K^{(*)}, \phi\}\ell^+\ell^-$*, *JHEP* **02** (2021) 088 [arXiv:2011.09813] [INSPIRE].

[15] ALEPH et al. collaborations, *Electroweak measurements in electron-positron collisions at W-boson-pair energies at LEP*, *Phys. Rept.* **532** (2013) 119 [arXiv:1302.3415] [INSPIRE].

JHEP07(2025)198

[16] PIENU collaboration, *Improved measurement of the $\pi \to e\nu$ branching ratio*, *Phys. Rev. Lett.* **115** (2015) 071801 [arXiv:1506.05845] [INSPIRE].

[17] NA62 collaboration, *Precision measurement of the ratio of the charged kaon leptonic decay rates*, *Phys. Lett. B* **719** (2013) 326 [arXiv:1212.4012] [INSPIRE].

[18] KEDR collaboration, *Measurement of the ratio of the leptonic widths $\Gamma_{ee}/\Gamma_{\mu\mu}$ for the J/ψ meson*, *Phys. Lett. B* **731** (2014) 227 [arXiv:1311.5005] [INSPIRE].

[19] ALEPH et al. collaborations, *Precision electroweak measurements on the Z resonance*, *Phys. Rept.* **427** (2006) 257 [hep-ex/0509008] [INSPIRE].

[20] M. Bordone, G. Isidori and A. Pattori, *On the Standard Model predictions for R_K and R_{K^*}*, *Eur. Phys. J. C* **76** (2016) 440 [arXiv:1605.07633] [INSPIRE].

[21] G. Isidori, D. Lancierini, S. Nabeebaccus and R. Zwicky, *QED in $\overline{B} \to \overline{K}\ell^+\ell^-$ LFU ratios: theory versus experiment, a Monte Carlo study*, *JHEP* **10** (2022) 146 [arXiv:2205.08635] [INSPIRE].

[22] G. Hiller and F. Krüger, *More model-independent analysis of $b \to s$ processes*, *Phys. Rev. D* **69** (2004) 074020 [hep-ph/0310219] [INSPIRE].

[23] I. Doršner et al., *Physics of leptoquarks in precision experiments and at particle colliders*, *Phys. Rept.* **641** (2016) 1 [arXiv:1603.04993] [INSPIRE].

[24] W. Altmannshofer, S. Gori, M. Pospelov and I. Yavin, *Quark flavor transitions in L_μ-L_τ models*, *Phys. Rev. D* **89** (2014) 095033 [arXiv:1403.1269] [INSPIRE].

[25] BABAR collaboration, *Measurement of branching fractions and rate asymmetries in the rare decays $B \to K^{(*)}\ell^+\ell^-$*, *Phys. Rev. D* **86** (2012) 032012 [arXiv:1204.3933] [INSPIRE].

[26] BELLE collaboration, *Test of lepton flavor universality and search for lepton flavor violation in $B \to K\ell\ell$ decays*, *JHEP* **03** (2021) 105 [arXiv:1908.01848] [INSPIRE].

[27] CMS collaboration, *Test of lepton flavor universality in $B^\pm \to K^\pm\mu^+\mu^-$ and $B^\pm \to K^\pm e^+e^-$ decays in proton-proton collisions at $\sqrt{s} = 13$ TeV*, *Rept. Prog. Phys.* **87** (2024) 077802 [arXiv:2401.07090] [INSPIRE].

[28] LHCb collaboration, *Tests of lepton universality using $B^0 \to K^0_S\ell^+\ell^-$ and $B^+ \to K^{*+}\ell^+\ell^-$ decays*, *Phys. Rev. Lett.* **128** (2022) 191802 [arXiv:2110.09501] [INSPIRE].

[29] LHCb collaboration, *Measurement of lepton universality parameters in $B^+ \to K^+\ell^+\ell^-$ and $B^0 \to K^{*0}\ell^+\ell^-$ decays*, *Phys. Rev. D* **108** (2023) 032002 [arXiv:2212.09153] [INSPIRE].

[30] LHCb collaboration, *Test of lepton universality in $b \to s\ell^+\ell^-$ decays*, *Phys. Rev. Lett.* **131** (2023) 051803 [arXiv:2212.09152] [INSPIRE].

[31] LHCb collaboration, *Test of lepton flavour universality with $B^0_s \to \phi\ell^+\ell^-$ decays*, *Phys. Rev. Lett.* **134** (2025) 121803 [arXiv:2410.13748] [INSPIRE].

[32] LHCb collaboration, *Test of lepton universality using $\Lambda^0_b \to pK^-\ell^+\ell^-$ decays*, *JHEP* **05** (2020) 040 [arXiv:1912.08139] [INSPIRE].

[33] LHCb collaboration, *Test of lepton flavour universality with $B^+ \to K^+\pi^+\pi^-\ell^+\ell^-$ decays*, *Phys. Rev. Lett.* **134** (2025) 181803 [arXiv:2412.11645] [INSPIRE].

[34] LHCb collaboration, *The LHCb detector at the LHC*, 2008 *JINST* **3** S08005 [INSPIRE].

[35] LHCb collaboration, *LHCb detector performance*, *Int. J. Mod. Phys. A* **30** (2015) 1530022 [arXiv:1412.6352] [INSPIRE].

JHEP07(2025)198

[36] R. Aaij et al., *Performance of the LHCb Vertex Locator*, 2014 *JINST* **9** P09007 [arXiv:1405.7808] [INSPIRE].

[37] LHCb Outer Tracker Group collaboration, *Performance of the LHCb Outer Tracker*, 2014 *JINST* **9** P01002 [arXiv:1311.3893] [INSPIRE].

[38] LHCb Outer Tracker Group collaboration, *Improved performance of the LHCb Outer Tracker in LHC Run 2*, 2017 *JINST* **12** P11016 [arXiv:1708.00819] [INSPIRE].

[39] LHCb RICH Group collaboration, *Performance of the LHCb RICH detector at the LHC*, *Eur. Phys. J. C* **73** (2013) 2431 [arXiv:1211.6759] [INSPIRE].

[40] A.A. Alves Jr. et al., *Performance of the LHCb muon system*, 2013 *JINST* **8** P02022 [arXiv:1211.1346] [INSPIRE].

[41] R. Aaij et al., *The LHCb trigger and its performance in 2011*, 2013 *JINST* **8** P04022 [arXiv:1211.3055] [INSPIRE].

[42] T. Sjöstrand, S. Mrenna and P.Z. Skands, *PYTHIA 6.4 physics and manual*, *JHEP* **05** (2006) 026 [hep-ph/0603175] [INSPIRE].

[43] LHCb collaboration, *Handling of the generation of primary events in Gauss, the LHCb simulation framework*, *J. Phys. Conf. Ser.* **331** (2011) 032047 [INSPIRE].

[44] D.J. Lange, *The EvtGen particle decay simulation package*, *Nucl. Instrum. Meth. A* **462** (2001) 152 [INSPIRE].

[45] P. Golonka and Z. Was, *PHOTOS Monte Carlo: A precision tool for QED corrections in Z and W decays*, *Eur. Phys. J. C* **45** (2006) 97 [hep-ph/0506026] [INSPIRE].

[46] J. Allison et al., *Geant4 developments and applications*, *IEEE Trans. Nucl. Sci.* **53** (2006) 270 [INSPIRE].

[47] LHCb collaboration, *The LHCb simulation application, Gauss: Design, evolution and experience*, *J. Phys. Conf. Ser.* **331** (2011) 032023 [INSPIRE].

[48] R. Brun and F. Rademakers, *ROOT: An object oriented data analysis framework*, *Nucl. Instrum. Meth. A* **389** (1997) 81 [INSPIRE].

[49] W. Verkerke and D.P. Kirkby, *The RooFit toolkit for data modeling*, *eConf C* **0303241** (2003) MOLT007 [physics/0306116] [INSPIRE].

[50] E. Rodrigues et al., *The Scikit HEP Project — overview and prospects*, *EPJ Web Conf.* **245** (2020) 06028 [arXiv:2007.03577] [INSPIRE].

[51] J. Pivarski et al., *Uproot*, DOI:10.5281/zenodo.4340632.

[52] A. Novak, H. Schreiner, M. Feickert and J. Eschle, *mplhep*, Apr., (2020) DOI:10.5281/zenodo.6807166.

[53] H. Schreiner, S. Liu and A. Goel, *hist*, DOI:10.5281/zenodo.4057112.

[54] H. Schreiner, H. Dembinski, S. Liu and J. Pivarski, *Boost-histogram: High-Performance Histograms as Objects*, (2020), pp. 63–69, [DOI:10.25080/majora-342d178e-009].

[55] E. Rodrigues and H. Schreiner, *scikit-hep/particle*, DOI:10.5281/zenodo.2552429.

[56] J. Eschle et al., *zfit: scalable pythonic fitting*, DOI:10.5281/zenodo.2602042.

[57] J. Eschle, A. Puig Navarro, R. Silva Coutinho and N. Serra, *zfit: Scalable pythonic fitting*, arXiv:1910.13429 [DOI:10.1016/j.softx.2020.100508] [INSPIRE].

JHEP07(2025)198

[58] LHCb collaboration, *LHCb calorimeters: Technical Design Report*, CERN-LHCC-2000-036 (2000) [INSPIRE].

[59] O. Deschamps et al., *Photon and neutral pion reconstruction*, LHCb-2003-091 (2003) [INSPIRE].

[60] Particle Data Group collaboration, *Review of particle physics*, *Phys. Rev. D* **110** (2024) 030001 [INSPIRE].

[61] T. Chen and C. Guestrin, *XGBoost: A scalable tree boosting system*, arXiv:1603.02754 [DOI:10.1145/2939672.2939785] [INSPIRE].

[62] LHCb collaboration, *Measurement of the phase difference between the short- and long-distance amplitudes in the $B^+ \to K^+\mu^+\mu^-$ decay*, *Eur. Phys. J. C* **77** (2017) 161 [arXiv:1612.06764] [INSPIRE].

[63] W.D. Hulsbergen, *Decay chain fitting with a Kalman filter*, *Nucl. Instrum. Meth. A* **552** (2005) 566 [physics/0503191] [INSPIRE].

[64] LHCb collaboration, *Test of lepton universality in beauty-quark decays*, *Nature Phys.* **18** (2022) 277 [arXiv:2103.11769] [INSPIRE].

[65] LHCb collaboration, *Measurements of the branching fraction ratio $\mathcal{B}(\phi \to \mu^+\mu^-)/\mathcal{B}(\phi \to e^+e^-)$ with charm meson decays*, *JHEP* **05** (2024) 293 [arXiv:2402.01336] [INSPIRE].

[66] LHCb collaboration, *Measurement of the electron reconstruction efficiency at LHCb*, 2019 *JINST* **14** P11023 [arXiv:1909.02957] [INSPIRE].

[67] L. Anderlini et al., *The PIDCalib package*, LHCb-PUB-2016-021 (2016) [INSPIRE].

[68] R. Aaij et al., *Selection and processing of calibration samples to measure the particle identification performance of the LHCb experiment in Run 2*, *EPJ Tech. Instrum.* **6** (2019) 1 [arXiv:1803.00824] [INSPIRE].

[69] M. Pivk and F.R. Le Diberder, *sPlot: A statistical tool to unfold data distributions*, *Nucl. Instrum. Meth. A* **555** (2005) 356 [physics/0402083] [INSPIRE].

[70] A. Rogozhnikov, *Reweighting with boosted decision trees*, *J. Phys. Conf. Ser.* **762** (2016) 012036 [arXiv:1608.05806] [INSPIRE].

[71] T. Skwarnicki, *A study of the radiative cascade transitions between the Upsilon-prime and Upsilon resonances*, Ph.D. thesis, Cracow, INP, Poland (1986) [INSPIRE].

[72] P. Ball and R. Zwicky, *New results on $B \to \pi, K, \eta$ decay form factors from light-cone sum rules*, *Phys. Rev. D* **71** (2005) 014015 [hep-ph/0406232] [INSPIRE].

[73] LHCb collaboration, *Measurements of the S-wave fraction in $B^0 \to K^+\pi^-\mu^+\mu^-$ decays and the $B^0 \to K^*(892)^0\mu^+\mu^-$ differential branching fraction*, *JHEP* **11** (2016) 047 [*Erratum ibid.* **04** (2017) 142] [arXiv:1606.04731] [INSPIRE].

[74] LHCb collaboration, *Search for the lepton-flavour violating decays $B^+ \to K^+\mu^\pm e^\mp$*, *Phys. Rev. Lett.* **123** (2019) 231802 [arXiv:1905.09244] [INSPIRE].

[75] B. Efron, *Bootstrap Methods: Another Look at the Jackknife*, *Annals Statist.* **7** (1979) 1 [INSPIRE].

JHEP07(2025)198

The LHCb collaboration

R. Aaij[38], A.S.W. Abdelmotteleb[57], C. Abellan Beteta[51], F. Abudinén[57], T. Ackernley[61], A.A. Adefisoye[69], B. Adeva[47], M. Adinolfi[55], P. Adlarson[83], C. Agapopoulou[14], C.A. Aidala[85], Z. Ajaltouni[11], S. Akar[11], K. Akiba[38], P. Albicocco[28], J. Albrecht[19,e], F. Alessio[49], Z. Aliouche[63], P. Alvarez Cartelle[56], R. Amalric[16], S. Amato[3], J.L. Amey[55], Y. Amhis[14], L. An[6], L. Anderlini[27], M. Andersson[51], A. Andreianov[44], P. Andreola[51], M. Andreotti[26], D. Andreou[69], A. Anelli[31,o,49], D. Ao[7], F. Archilli[37,u], M. Argenton[26], S. Arguedas Cuendis[9,49], A. Artamonov[44], M. Artuso[69], E. Aslanides[13], R. Ataíde Da Silva[50], M. Atzeni[65], B. Audurier[12], D. Bacher[64], I. Bachiller Perea[10], S. Bachmann[22], M. Bachmayer[50], J.J. Back[57], P. Baladron Rodriguez[47], V. Balagura[15], A. Balboni[26], W. Baldini[26], L. Balzani[19], H. Bao[7], J. Baptista de Souza Leite[61], C. Barbero Pretel[47,12], M. Barbetti[27], I.R. Barbosa[70], R.J. Barlow[63], M. Barnyakov[25], S. Barsuk[14], W. Barter[59], J. Bartz[69], J.M. Basels[17], S. Bashir[40], B. Batsukh[5], P.B. Battista[14], A. Bay[50], A. Beck[65], M. Becker[19], F. Bedeschi[35], I.B. Bediaga[2], N.A. Behling[19], S. Belin[47], K. Belous[44], I. Belov[29], I. Belyaev[36], G. Benane[13], G. Bencivenni[28], E. Ben-Haim[16], A. Berezhnoy[44], R. Bernet[51], S. Bernet Andres[46], A. Bertolin[33], C. Betancourt[51], F. Betti[59], J. Bex[56], Ia. Bezshyiko[51], O. Bezshyyko[84], J. Bhom[41], M.S. Bieker[19], N.V. Biesuz[26], P. Billoir[16], A. Biolchini[38], M. Birch[62], F.C.R. Bishop[10], A. Bitadze[63], A. Bizzeti[], T. Blake[57], F. Blanc[50], J.E. Blank[19], S. Blusk[69], V. Bocharnikov[44], J.A. Boelhauve[19], O. Boente Garcia[15], T. Boettcher[68], A. Bohare[59], A. Boldyrev[44], C.S. Bolognani[80], R. Bolzonella[26], R.B. Bonacci[1], N. Bondar[44,49], A. Bordelius[49], F. Borgato[33,49], S. Borghi[63], M. Borsato[31,o], J.T. Borsuk[81], E. Bottalico[61], S.A. Bouchiba[50], M. Bovill[64], T.J.V. Bowcock[61], A. Boyer[49], C. Bozzi[26], J.D. Brandenburg[86], A. Brea Rodriguez[50], N. Breer[19], J. Brodzicka[41], A. Brossa Gonzalo[47,†], J. Brown[61], D. Brundu[32], E. Buchanan[59], L. Buonincontri[33,p], M. Burgos Marcos[80], A.T. Burke[63], C. Burr[49], J.S. Butter[56], J. Buytaert[49], W. Byczynski[49], S. Cadeddu[32], H. Cai[74], A. Caillet[16], R. Calabrese[26,k], S. Calderon Ramirez[9], L. Calefice[45], S. Cali[28], M. Calvi[31,o], M. Calvo Gomez[46], P. Camargo Magalhaes[2,z], J.I. Cambon Bouzas[47], P. Campana[28], D.H. Campora Perez[80], A.F. Campoverde Quezada[7], S. Capelli[31], L. Capriotti[26], R. Caravaca-Mora[9], A. Carbone[25,i], L. Carcedo Salgado[47], R. Cardinale[29,m], A. Cardini[32], P. Carniti[31,o], L. Carus[22], A. Casais Vidal[65], R. Caspary[22], G. Casse[61], M. Cattaneo[49], G. Cavallero[26,49], V. Cavallini[26,k], S. Celani[22], S. Cesare[30,n], A.J. Chadwick[61], I. Chahrour[85], H. Chang[4,b], M. Charles[16], Ph. Charpentier[49], E. Chatzianagnostou[38], M. Chefdeville[10], C. Chen[56], S. Chen[5], Z. Chen[7], A. Chernov[41], S. Chernyshenko[53], X. Chiotopoulos[80], V. Chobanova[82], M. Chrzaszcz[41], A. Chubykin[44], V. Chulikov[28,36], P. Ciambrone[28], X. Cid Vidal[47], G. Ciezarek[49], P. Cifra[49], P.E.L. Clarke[59], M. Clemencic[49], H.V. Cliff[56], J. Closier[49], C. Cocha Toapaxi[22], V. Coco[49], J. Cogan[13], E. Cogneras[11], L. Cojocariu[43], S. Collaviti[50], P. Collins[49], T. Colombo[49], M. Colonna[19], A. Comerma-Montells[45], L. Congedo[24], A. Contu[32], N. Cooke[60], C. Coronel[66], I. Corredoira [12], A. Correia[16], G. Corti[49], J. Cottee Meldrum[55], B. Couturier[49], D.C. Craik[51], M. Cruz Torres[2,f], E. Curras Rivera[50], R. Currie[59], C.L. Da Silva[68], S. Dadabaev[44], L. Dai[71], X. Dai[4], E. Dall'Occo[49], J. Dalseno[82], C. D'Ambrosio[49],

JHEP07(2025)198

J. Daniel[11], P. d'Argent[24], G. Darze[3], A. Davidson[57], J.E. Davies[63], O. De Aguiar Francisco[63], C. De Angelis[32,j], F. De Benedetti[49], J. de Boer[38], K. De Bruyn[79], S. De Capua[63], M. De Cian[22], U. De Freitas Carneiro Da Graca[2,a], E. De Lucia[28], J.M. De Miranda[2], L. De Paula[3], M. De Serio[24,g], P. De Simone[28], F. De Vellis[19], J.A. de Vries[80], F. Debernardis[24], D. Decamp[10], V. Dedu[13], S. Dekkers[1], L. Del Buono[16], B. Delaney[65], H.-P. Dembinski[19], J. Deng[8], V. Denysenko[51], O. Deschamps[11], F. Dettori[32,j], B. Dey[77], P. Di Nezza[28], I. Diachkov[44], S. Didenko[44], S. Ding[69], L. Dittmann[22], V. Dobishuk[53], A.D. Docheva[60], C. Dong[4,b], A.M. Donohoe[23], F. Dordei[32], A.C. dos Reis[2], A.D. Dowling[69], W. Duan[72], P. Duda[81], M.W. Dudek[41], L. Dufour[49], V. Duk[34], P. Durante[49], M.M. Duras[81], J.M. Durham[68], O.D. Durmus[77], A. Dziurda[41], A. Dzyuba[44], S. Easo[58], E. Eckstein[18], U. Egede[1], A. Egorychev[44], V. Egorychev[44], S. Eisenhardt[59], E. Ejopu[63], L. Eklund[83], M. Elashri[66], J. Ellbracht[19], S. Ely[62], A. Ene[43], J. Eschle[69], S. Esen[22], T. Evans[38], F. Fabiano[32], S. Faghih[66], L.N. Falcao[2], Y. Fan[7], B. Fang[7], L. Fantini[34,q,49], M. Faria[50], K. Farmer[59], D. Fazzini[31,o], L. Felkowski[81], M. Feng[5,7], M. Feo[2], A. Fernandez Casani[48], M. Fernandez Gomez[47], A.D. Fernez[67], F. Ferrari[25,i], F. Ferreira Rodrigues[3], M. Ferrillo[51], M. Ferro-Luzzi[49], S. Filippov[44], R.A. Fini[24], M. Fiorini[26,k], M. Firlej[40], K.L. Fischer[64], D.S. Fitzgerald[85], C. Fitzpatrick[63], T. Fiutowski[40], F. Fleuret[15], M. Fontana[25], L.F. Foreman[63], R. Forty[49], D. Foulds-Holt[56], V. Franco Lima[3], M. Franco Sevilla[67], M. Frank[49], E. Franzoso[26,k], G. Frau[63], C. Frei[49], D.A. Friday[63], J. Fu[7], Q. Führing[19,e,56], Y. Fujii[1], T. Fulghesu[13], E. Gabriel[38], G. Galati[24], M.D. Galati[38], A. Gallas Torreira[47], D. Galli[25,i], S. Gambetta[59], M. Gandelman[3], P. Gandini[30], B. Ganie[63], H. Gao[7], R. Gao[64], T.Q. Gao[56], Y. Gao[8], Y. Gao[6], Y. Gao[8], L.M. Garcia Martin[50], P. Garcia Moreno[45], J. García Pardiñas[49], P. Gardner[67], K.G. Garg[8], L. Garrido[45], C. Gaspar[49], A. Gavrikov[33], L.L. Gerken[19], E. Gersabeck[63], M. Gersabeck[20], T. Gershon[57], S. Ghizzo[29,m], Z. Ghorbanimoghaddam[55], L. Giambastiani[33,p], F.I. Giasemis[16,d], V. Gibson[56], H.K. Giemza[42], A.L. Gilman[64], M. Giovannetti[28], A. Gioventù[45], L. Girardey[63,58], C. Giugliano[26,k], M.A. Giza[41], F.C. Glaser[14,22], V.V. Gligorov[16,49], C. Göbel[70], L. Golinka-Bezshyyko[84], E. Golobardes[46], D. Golubkov[44], A. Golutvin[62,49], S. Gomez Fernandez[45], W. Gomulka[40], F. Goncalves Abrantes[64], M. Goncerz[41], G. Gong[4,b], J.A. Gooding[19], I.V. Gorelov[44], C. Gotti[31], E. Govorkova[65], J.P. Grabowski[18], L.A. Granado Cardoso[49], E. Graugés[45], E. Graverini[50,s], L. Grazette[57], G. Graziani[], A.T. Grecu[43], L.M. Greeven[38], N.A. Grieser[66], L. Grillo[60], S. Gromov[44], C. Gu[15], M. Guarise[26], L. Guerry[11], V. Guliaeva[44], P.A. Günther[22], A.-K. Guseinov[50], E. Gushchin[44], Y. Guz[6,49], T. Gys[49], K. Habermann[18], T. Hadavizadeh[1], C. Hadjivasiliou[67], G. Haefeli[50], C. Haen[49], G. Hallett[57], M.M. Halvorsen[49], P.M. Hamilton[67], J. Hammerich[61], Q. Han[33], X. Han[22,49], S. Hansmann-Menzemer[22], L. Hao[7], N. Harnew[64], T.H. Harris[1], M. Hartmann[14], S. Hashmi[40], J. He[7,c], F. Hemmer[49], C. Henderson[66], R.D.L. Henderson[1,57], A.M. Hennequin[49], K. Hennessy[61], L. Henry[50], J. Herd[62], P. Herrero Gascon[22], J. Heuel[17], A. Hicheur[3], G. Hijano Mendizabal[51], J. Horswill[63], R. Hou[8], Y. Hou[11], N. Howarth[61], J. Hu[72], W. Hu[6], X. Hu[4,b], W. Huang[7], W. Hulsbergen[38], R.J. Hunter[57], M. Hushchyn[44], D. Hutchcroft[61], M. Idzik[40], D. Ilin[44],

JHEP07(2025)198

P. Ilten[66], A. Inglessi[44], A. Iniukhin[44], A. Ishteev[44], K. Ivshin[44], R. Jacobsson[49], H. Jage[17], S.J. Jaimes Elles[75,49,48], S. Jakobsen[49], E. Jans[38], B.K. Jashal[48], A. Jawahery[67], V. Jevtic[19,e], E. Jiang[67], X. Jiang[5,7], Y. Jiang[7], Y.J. Jiang[6], M. John[64], A. John Rubesh Rajan[23], D. Johnson[54], C.R. Jones[56], T.P. Jones[57], S. Joshi[42], B. Jost[49], J. Juan Castella[56], N. Jurik[49], I. Juszczak[41], D. Kaminaris[50], S. Kandybei[52], M. Kane[59], Y. Kang[4,b], C. Kar[11], M. Karacson[49], D. Karpenkov[44], A. Kauniskangas[50], J.W. Kautz[66], M.K. Kazanecki[41], F. Keizer[49], M. Kenzie[56], T. Ketel[38], B. Khanji[69], A. Kharisova[44], S. Kholodenko[35,49], G. Khreich[14], T. Kirn[17], V.S. Kirsebom[31,o], O. Kitouni[65], S. Klaver[39], N. Kleijne[35,r], K. Klimaszewski[42], M.R. Kmiec[42], S. Koliiev[53], L. Kolk[19], A. Konoplyannikov[6], P. Kopciewicz[49], P. Koppenburg[38], A. Korchin[52], M. Korolev[44], I. Kostiuk[38], O. Kot[53], S. Kotriakhova, A. Kozachuk[44], P. Kravchenko[44], L. Kravchuk[44], M. Kreps[57], P. Krokovny[44], W. Krupa[69], W. Krzemien[42], O. Kshyvanskyi[53], S. Kubis[81], M. Kucharczyk[41], V. Kudryavtsev[44], E. Kulikova[44], A. Kupsc[83], V. Kushnir[52], B. Kutsenko[13], I. Kyryllin[52], D. Lacarrere[49], P. Laguarta Gonzalez[45], A. Lai[32], A. Lampis[32], D. Lancierini[62,*], C. Landesa Gomez[47], J.J. Lane[1], R. Lane[55], G. Lanfranchi[28], C. Langenbruch[22], J. Langer[19], O. Lantwin[44], T. Latham[57], F. Lazzari[35,s,49], C. Lazzeroni[54], R. Le Gac[13], H. Lee[61], R. Lefèvre[11], A. Leflat[44], S. Legotin[44], M. Lehuraux[57], E. Lemos Cid[49], O. Leroy[13], T. Lesiak[41], E.D. Lesser[49], B. Leverington[22], A. Li[4,b], C. Li[4], C. Li[13], H. Li[72], J. Li[8], K. Li[8], L. Li[63], M. Li[8], P. Li[7], P.-R. Li[73], Q. Li[5,7], S. Li[8], T. Li[71], T. Li[72], Y. Li[8], Y. Li[5], Z. Lian[4,b], X. Liang[69], S. Libralon[48], C. Lin[7], T. Lin[58], R. Lindner[49], H. Linton[62], V. Lisovskyi[50], R. Litvinov[32,49], D. Liu[8], F.L. Liu[1], G. Liu[72], K. Liu[73], S. Liu[5,7], W. Liu[8], Y. Liu[59], Y. Liu[73], Y.L. Liu[62], G. Loachamin Ordonez[70], A. Lobo Salvia[45], A. Loi[32], T. Long[56], J.H. Lopes[3], A. Lopez Huertas[45], S. López Soliño[47], Q. Lu[15], C. Lucarelli[27,l], D. Lucchesi[33,p], M. Lucio Martinez[80], V. Lukashenko[38,53], Y. Luo[6], A. Lupato[33,h], E. Luppi[26,k], K. Lynch[23], X.-R. Lyu[7], G.M. Ma[4,b], S. Maccolini[19], F. Machefert[14], F. Maciuc[43], B. Mack[69], I. Mackay[64], L.M. Mackey[69], L.R. Madhan Mohan[56], M.J. Madurai[54], A. Maevskiy[44], D. Magdalinski[38], D. Maisuzenko[44], J.J. Malczewski[41], S. Malde[64], L. Malentacca[49], A. Malinin[44], T. Maltsev[44], G. Manca[32,j], G. Mancinelli[13], C. Mancuso[30], R. Manera Escalero[45], F.M. Manganella[37], D. Manuzzi[25], D. Marangotto[30], J.F. Marchand[10], R. Marchevski[50], U. Marconi[25], E. Mariani[16], S. Mariani[49], C. Marin Benito[45], J. Marks[22], A.M. Marshall[55], L. Martel[64], G. Martelli[34,q], G. Martellotti[36], L. Martinazzoli[49], M. Martinelli[31,o], D. Martinez Gomez[79], D. Martinez Santos[82], F. Martinez Vidal[48], A. Martorell i Granollers[46], A. Massafferri[2], R. Matev[49], A. Mathad[49], V. Matiunin[44], C. Matteuzzi[69], K.R. Mattioli[15], A. Mauri[62], E. Maurice[15], J. Mauricio[45], P. Mayencourt[50], J. Mazorra de Cos[48], M. Mazurek[42], M. McCann[62], T.H. McGrath[63], N.T. McHugh[60], A. McNab[63], R. McNulty[23], B. Meadows[66], G. Meier[19], D. Melnychuk[42], F.M. Meng[4,b], M. Merk[38,80], A. Merli[50], L. Meyer Garcia[67], D. Miao[5,7], H. Miao[7], M. Mikhasenko[76], D.A. Milanes[75,x], A. Minotti[31,o], E. Minucci[28], T. Miralles[11], B. Mitreska[19], D.S. Mitzel[19], A. Modak[58], L. Moeser[19], R.A. Mohammed[64], R.D. Moise[17], E.F. Molina Cardenas[85], T. Mombächer[49], M. Monk[57,1], S. Monteil[11], A. Morcillo Gomez[47], G. Morello[28], M.J. Morello[35,r],

JHEP07(2025)198

M.P. Morgenthaler[22], J. Moron[40], W. Morren[38], A.B. Morris[49], A.G. Morris[13], R. Mountain[69], H. Mu[4,b], Z.M. Mu[6], E. Muhammad[57], F. Muheim[59], M. Mulder[79], K. Müller[51], F. Muñoz-Rojas[9], R. Murta[62], V. Mytrochenko[52], P. Naik[61], T. Nakada[50], R. Nandakumar[58], T. Nanut[49], I. Nasteva[3], M. Needham[59], E. Nekrasova[44], N. Neri[30,n], S. Neubert[18], N. Neufeld[49], P. Neustroev[44], J. Nicolini[49], D. Nicotra[80], E.M. Niel[49], N. Nikitin[44], Q. Niu[73], P. Nogarolli[3], P. Nogga[18], C. Normand[55], J. Novoa Fernandez[47], G. Nowak[66], C. Nunez[85], H.N. Nur[60], A. Oblakowska-Mucha[40], V. Obraztsov[44], T. Oeser[17], S. Okamura[26,k], A. Okhotnikov[44], O. Okhrimenko[53], R. Oldeman[32,j], F. Oliva[59], M. Olocco[19], C.J.G. Onderwater[80], R.H. O'Neil[49], D. Osthues[19], J.M. Otalora Goicochea[3], P. Owen[51], A. Oyanguren[48], O. Ozcelik[59], F. Paciolla[35,v], A. Padee[42], K.O. Padeken[18], B. Pagare[57], T. Pajero[49], A. Palano[24], M. Palutan[28], X. Pan[4,b], G. Panshin[5], L. Paolucci[57], A. Papanestis[58,49], M. Pappagallo[24,g], L.L. Pappalardo[26], C. Pappenheimer[66], C. Parkes[63], D. Parmar[76], B. Passalacqua[26,k], G. Passaleva[27], D. Passaro[35,r,49], A. Pastore[24], M. Patel[62], J. Patoc[64], C. Patrignani[25,i], A. Paul[69], C.J. Pawley[80], A. Pellegrino[38], J. Peng[5,7], M. Pepe Altarelli[28], S. Perazzini[25], D. Pereima[44], H. Pereira Da Costa[68], A. Pereiro Castro[47], P. Perret[11], A. Perrevoort[79], A. Perro[49,13], M.J. Peters[66], K. Petridis[55], A. Petrolini[29,m], J.P. Pfaller[66], H. Pham[69], L. Pica[35], M. Piccini[34], L. Piccolo[32], B. Pietrzyk[10], G. Pietrzyk[14], R.N. Pilato[61], D. Pinci[36], F. Pisani[49], M. Pizzichemi[31,o,49], V.M. Placinta[43], M. Plo Casasus[47], T. Poeschl[49], F. Polci[16], M. Poli Lener[28], A. Poluektov[13], N. Polukhina[44], I. Polyakov[63], E. Polycarpo[3], S. Ponce[49], D. Popov[7,49], S. Poslavskii[44], K. Prasanth[59], C. Prouve[82], D. Provenzano[32,j], V. Pugatch[53], G. Punzi[35,s], S. Qasim[51], Q.Q. Qian[6], W. Qian[7], N. Qin[4,b], S. Qu[4,b], R. Quagliani[49], R.I. Rabadan Trejo[57], J.H. Rademacker[55], M. Rama[35], M. Ramírez García[85], V. Ramos De Oliveira[70], M. Ramos Pernas[57], M.S. Rangel[3], F. Ratnikov[44], G. Raven[39], M. Rebollo De Miguel[48], F. Redi[30,h], J. Reich[55], F. Reiss[20], Z. Ren[7], P.K. Resmi[64], M. Ribalda Galvez[45], R. Ribatti[50], G. Ricart[15,12], D. Riccardi[35,r], S. Ricciardi[58], K. Richardson[65], M. Richardson-Slipper[59], K. Rinnert[61], P. Robbe[14,49], G. Robertson[60], E. Rodrigues[61], A. Rodriguez Alvarez[45], E. Rodriguez Fernandez[47], J.A. Rodriguez Lopez[75], E. Rodriguez Rodriguez[49], J. Roensch[19], A. Rogachev[44], A. Rogovskiy[58], D.L. Rolf[19], P. Roloff[49], V. Romanovskiy[66], A. Romero Vidal[47], G. Romolini[26], F. Ronchetti[50], T. Rong[6], M. Rotondo[28], S.R. Roy[22], M.S. Rudolph[69], M. Ruiz Diaz[22], R.A. Ruiz Fernandez[47], J. Ruiz Vidal[80], J. Ryzka[40], J.J. Saavedra-Arias[9], J.J. Saborido Silva[47], R. Sadek[15], N. Sagidova[44], D. Sahoo[77], N. Sahoo[54], B. Saitta[32,j], M. Salomoni[31,49,o], I. Sanderswood[48], R. Santacesaria[36], C. Santamarina Rios[47], M. Santimaria[28], L. Santoro[2], E. Santovetti[37], A. Saputi[26,49], D. Saranin[44], A. Sarnatskiy[79], G. Sarpis[59], M. Sarpis[78], C. Satriano[36,t], A. Satta[37], M. Saur[73], D. Savrina[44], H. Sazak[17], F. Sborzacchi[49,28], A. Scarabotto[19], S. Schael[17], S. Scherl[61], M. Schiller[60], H. Schindler[49], M. Schmelling[21], B. Schmidt[49], S. Schmitt[17], H. Schmitz[18], O. Schneider[50], A. Schopper[62], N. Schulte[19], S. Schulte[50], M.H. Schune[14], G. Schwering[17], B. Sciascia[28], A. Sciuccati[49], I. Segal[76], S. Sellam[47], A. Semennikov[44], T. Senger[51], M. Senghi Soares[39], A. Sergi[29,m], N. Serra[51], L. Sestini[27], A. Seuthe[19], Y. Shang[6], D.M. Shangase[85], M. Shapkin[44], R.S. Sharma[69], I. Shchemerov[44], L. Shchutska[50], T. Shears[61], L. Shekhtman[44], Z. Shen[38], S. Sheng[5,7],

JHEP07(2025)198

V. Shevchenko[44], B. Shi[7], Q. Shi[7], Y. Shimizu[14], E. Shmanin[25], R. Shorkin[44], J.D. Shupperd[69], R. Silva Coutinho[69], G. Simi[33,p], S. Simone[24,g], M. Singha[77], N. Skidmore[57], T. Skwarnicki[69], M.W. Slater[54], E. Smith[65], K. Smith[68], M. Smith[62], A. Snoch[38], L. Soares Lavra[59], M.D. Sokoloff[66], F.J.P. Soler[60], A. Solomin[55], A. Solovev[44], I. Solovyev[44], N.S. Sommerfeld[18], R. Song[1], Y. Song[50], Y. Song[4,b], Y.S. Song[6], F.L. Souza De Almeida[69], B. Souza De Paula[3], E. Spadaro Norella[29,m], E. Spedicato[25], J.G. Speer[19], E. Spiridenkov[44], P. Spradlin[60], V. Sriskaran[49], F. Stagni[49], M. Stahl[76], S. Stahl[49], S. Stanislaus[64], M. Stefaniak[86], E.N. Stein[49], O. Steinkamp[51], O. Stenyakin[44], H. Stevens[19], D. Strekalina[44], Y. Su[7], F. Suljik[64], J. Sun[32], L. Sun[74], D. Sundfeld[2], W. Sutcliffe[51], K. Swientek[40], F. Swystun[56], A. Szabelski[42], T. Szumlak[40], Y. Tan[4,b], Y. Tang[74], M.D. Tat[22], A. Terentev[44], F. Terzuoli[35,v,49], F. Teubert[49], E. Thomas[49], D.J.D. Thompson[54], H. Tilquin[62], V. Tisserand[11], S. T'Jampens[10], M. Tobin[5,49], L. Tomassetti[26,k], G. Tonani[30,n], X. Tong[6], T. Tork[30], D. Torres Machado[2], L. Toscano[19], D.Y. Tou[4,b], C. Trippl[46], G. Tuci[22], N. Tuning[38], L.H. Uecker[22], A. Ukleja[40], D.J. Unverzagt[22], A. Upadhyay[77], B. Urbach[59], A. Usachov[39], A. Ustyuzhanin[44], U. Uwer[22], V. Vagnoni[25], V. Valcarce Cadenas[47], G. Valenti[25], N. Valls Canudas[49], J. van Eldik[49], H. Van Hecke[68], E. van Herwijnen[62], C.B. Van Hulse[47,y], R. Van Laak[50], M. van Veghel[38], G. Vasquez[51], R. Vazquez Gomez[45], P. Vazquez Regueiro[47], C. Vázquez Sierra[82], S. Vecchi[26], J.J. Velthuis[55], M. Veltri[27,w], A. Venkateswaran[50], M. Verdoglia[32], M. Vesterinen[57], D. Vico Benet[64], P. Vidrier Villalba[45], M. Vieites Diaz[47], X. Vilasis-Cardona[46], E. Vilella Figueras[61], A. Villa[25], P. Vincent[16], B. Vivacqua[3], F.C. Volle[54], D. vom Bruch[13], N. Voropaev[44], K. Vos[80], C. Vrahas[59], J. Wagner[19], J. Walsh[35], E.J. Walton[1,57], G. Wan[6], A. Wang[7], C. Wang[22], G. Wang[8], H. Wang[73], J. Wang[6], J. Wang[5], J. Wang[4,b], J. Wang[74], M. Wang[49], N.W. Wang[7], R. Wang[55], X. Wang[8], X. Wang[72], X.W. Wang[62], Y. Wang[6], Y.W. Wang[73], Z. Wang[14], Z. Wang[4,b], Z. Wang[30], J.A. Ward[57,1], M. Waterlaat[49], N.K. Watson[54], D. Websdale[62], Y. Wei[6], J. Wendel[82], B.D.C. Westhenry[55], C. White[56], M. Whitehead[60], E. Whiter[54], A.R. Wiederhold[63], D. Wiedner[19], G. Wilkinson[64], M.K. Wilkinson[66], M. Williams[65], M.J. Williams[49], M.R.J. Williams[59], R. Williams[56], Z. Williams[55], F.F. Wilson[58], M. Winn[12], W. Wislicki[42], M. Witek[41], L. Witola[19], G. Wormser[14], S.A. Wotton[56], H. Wu[69], J. Wu[8], X. Wu[74], Y. Wu[6,56], Z. Wu[7], K. Wyllie[49], S. Xian[72], Z. Xiang[5], Y. Xie[8], T.X. Xing[30], A. Xu[35], L. Xu[4,b], L. Xu[4,b], M. Xu[57], Z. Xu[49], Z. Xu[7], Z. Xu[5], K. Yang[62], S. Yang[7], X. Yang[6], Y. Yang[29,m], Z. Yang[6], V. Yeroshenko[14], H. Yeung[63], H. Yin[8], X. Yin[7], C.Y. Yu[6], J. Yu[71], X. Yuan[5], Y Yuan[5,7], E. Zaffaroni[50], M. Zavertyaev[21], M. Zdybal[41], F. Zenesini[25], C. Zeng[5,7], M. Zeng[4,b], C. Zhang[6], D. Zhang[8], J. Zhang[7], L. Zhang[4,b], S. Zhang[71], S. Zhang[64], Y. Zhang[6], Y.Z. Zhang[4,b], Z. Zhang[4,b], Y. Zhao[22], A. Zhelezov[22], S.Z. Zheng[6], X.Z. Zheng[4,b], Y. Zheng[7], T. Zhou[6], X. Zhou[8], Y. Zhou[7], V. Zhovkovska[57], L.Z. Zhu[7], X. Zhu[4,b], X. Zhu[8], Y. Zhu[17], V. Zhukov[17], J. Zhuo[48], Q. Zou[5,7], D. Zuliani[33,p], G. Zunica[50]

[1] *School of Physics and Astronomy, Monash University, Melbourne, Australia*
[2] *Centro Brasileiro de Pesquisas Físicas (CBPF), Rio de Janeiro, Brazil*
[3] *Universidade Federal do Rio de Janeiro (UFRJ), Rio de Janeiro, Brazil*

JHEP07(2025)198

[4] Department of Engineering Physics, Tsinghua University, Beijing, China
[5] Institute Of High Energy Physics (IHEP), Beijing, China
[6] School of Physics State Key Laboratory of Nuclear Physics and Technology, Peking University, Beijing, China
[7] University of Chinese Academy of Sciences, Beijing, China
[8] Institute of Particle Physics, Central China Normal University, Wuhan, Hubei, China
[9] Consejo Nacional de Rectores (CONARE), San Jose, Costa Rica
[10] Université Savoie Mont Blanc, CNRS, IN2P3-LAPP, Annecy, France
[11] Université Clermont Auvergne, CNRS/IN2P3, LPC, Clermont-Ferrand, France
[12] Université Paris-Saclay, Centre d'Etudes de Saclay (CEA), IRFU, Saclay, France, Gif-Sur-Yvette, France
[13] Aix Marseille Univ, CNRS/IN2P3, CPPM, Marseille, France
[14] Université Paris-Saclay, CNRS/IN2P3, IJCLab, Orsay, France
[15] Laboratoire Leprince-Ringuet, CNRS/IN2P3, Ecole Polytechnique, Institut Polytechnique de Paris, Palaiseau, France
[16] LPNHE, Sorbonne Université, Paris Diderot Sorbonne Paris Cité, CNRS/IN2P3, Paris, France
[17] I. Physikalisches Institut, RWTH Aachen University, Aachen, Germany
[18] Universität Bonn – Helmholtz-Institut für Strahlen und Kernphysik, Bonn, Germany
[19] Fakultät Physik, Technische Universität Dortmund, Dortmund, Germany
[20] Physikalisches Institut, Albert-Ludwigs-Universität Freiburg, Freiburg, Germany
[21] Max-Planck-Institut für Kernphysik (MPIK), Heidelberg, Germany
[22] Physikalisches Institut, Ruprecht-Karls-Universität Heidelberg, Heidelberg, Germany
[23] School of Physics, University College Dublin, Dublin, Ireland
[24] INFN Sezione di Bari, Bari, Italy
[25] INFN Sezione di Bologna, Bologna, Italy
[26] INFN Sezione di Ferrara, Ferrara, Italy
[27] INFN Sezione di Firenze, Firenze, Italy
[28] INFN Laboratori Nazionali di Frascati, Frascati, Italy
[29] INFN Sezione di Genova, Genova, Italy
[30] INFN Sezione di Milano, Milano, Italy
[31] INFN Sezione di Milano-Bicocca, Milano, Italy
[32] INFN Sezione di Cagliari, Monserrato, Italy
[33] INFN Sezione di Padova, Padova, Italy
[34] INFN Sezione di Perugia, Perugia, Italy
[35] INFN Sezione di Pisa, Pisa, Italy
[36] INFN Sezione di Roma La Sapienza, Roma, Italy
[37] INFN Sezione di Roma Tor Vergata, Roma, Italy
[38] Nikhef National Institute for Subatomic Physics, Amsterdam, Netherlands
[39] Nikhef National Institute for Subatomic Physics and VU University Amsterdam, Amsterdam, Netherlands
[40] AGH – University of Krakow, Faculty of Physics and Applied Computer Science, Kraków, Poland
[41] Henryk Niewodniczanski Institute of Nuclear Physics Polish Academy of Sciences, Kraków, Poland
[42] National Center for Nuclear Research (NCBJ), Warsaw, Poland
[43] Horia Hulubei National Institute of Physics and Nuclear Engineering, Bucharest-Magurele, Romania
[44] Authors affiliated with an institute formerly covered by a cooperation agreement with CERN.
[45] ICCUB, Universitat de Barcelona, Barcelona, Spain
[46] La Salle, Universitat Ramon Llull, Barcelona, Spain
[47] Instituto Galego de Física de Altas Enerxías (IGFAE), Universidade de Santiago de Compostela, Santiago de Compostela, Spain
[48] Instituto de Fisica Corpuscular, Centro Mixto Universidad de Valencia – CSIC, Valencia, Spain
[49] European Organization for Nuclear Research (CERN), Geneva, Switzerland
[50] Institute of Physics, Ecole Polytechnique Fédérale de Lausanne (EPFL), Lausanne, Switzerland
[51] Physik-Institut, Universität Zürich, Zürich, Switzerland
[52] NSC Kharkiv Institute of Physics and Technology (NSC KIPT), Kharkiv, Ukraine
[53] Institute for Nuclear Research of the National Academy of Sciences (KINR), Kyiv, Ukraine

JHEP07(2025)198

[54] School of Physics and Astronomy, University of Birmingham, Birmingham, United Kingdom
[55] H.H. Wills Physics Laboratory, University of Bristol, Bristol, United Kingdom
[56] Cavendish Laboratory, University of Cambridge, Cambridge, United Kingdom
[57] Department of Physics, University of Warwick, Coventry, United Kingdom
[58] STFC Rutherford Appleton Laboratory, Didcot, United Kingdom
[59] School of Physics and Astronomy, University of Edinburgh, Edinburgh, United Kingdom
[60] School of Physics and Astronomy, University of Glasgow, Glasgow, United Kingdom
[61] Oliver Lodge Laboratory, University of Liverpool, Liverpool, United Kingdom
[62] Imperial College London, London, United Kingdom
[63] Department of Physics and Astronomy, University of Manchester, Manchester, United Kingdom
[64] Department of Physics, University of Oxford, Oxford, United Kingdom
[65] Massachusetts Institute of Technology, Cambridge, MA, United States
[66] University of Cincinnati, Cincinnati, OH, United States
[67] University of Maryland, College Park, MD, United States
[68] Los Alamos National Laboratory (LANL), Los Alamos, NM, United States
[69] Syracuse University, Syracuse, NY, United States
[70] Pontifícia Universidade Católica do Rio de Janeiro (PUC-Rio), Rio de Janeiro, Brazil, associated to [3]
[71] School of Physics and Electronics, Hunan University, Changsha City, China, associated to [8]
[72] Guangdong Provincial Key Laboratory of Nuclear Science, Guangdong-Hong Kong Joint Laboratory of Quantum Matter, Institute of Quantum Matter, South China Normal University, Guangzhou, China, associated to [4]
[73] Lanzhou University, Lanzhou, China, associated to [5]
[74] School of Physics and Technology, Wuhan University, Wuhan, China, associated to [4]
[75] Departamento de Fisica, Universidad Nacional de Colombia, Bogota, Colombia, associated to [16]
[76] Ruhr Universitaet Bochum, Fakultaet f. Physik und Astronomie, Bochum, Germany, associated to [19]
[77] Eotvos Lorand University, Budapest, Hungary, associated to [49]
[78] Faculty of Physics, Vilnius University, Vilnius, Lithuania, associated to [20]
[79] Van Swinderen Institute, University of Groningen, Groningen, Netherlands, associated to [38]
[80] Universiteit Maastricht, Maastricht, Netherlands, associated to [38]
[81] Tadeusz Kosciuszko Cracow University of Technology, Cracow, Poland, associated to [41]
[82] Universidade da Coruña, A Coruña, Spain, associated to [46]
[83] Department of Physics and Astronomy, Uppsala University, Uppsala, Sweden, associated to [60]
[84] Taras Schevchenko University of Kyiv, Faculty of Physics, Kyiv, Ukraine, associated to [14]
[85] University of Michigan, Ann Arbor, MI, United States, associated to [69]
[86] Ohio State University, Columbus, United States, associated to [68]

[a] Centro Federal de Educacão Tecnológica Celso Suckow da Fonseca, Rio De Janeiro, Brazil
[b] Center for High Energy Physics, Tsinghua University, Beijing, China
[c] Hangzhou Institute for Advanced Study, UCAS, Hangzhou, China
[d] LIP6, Sorbonne Université, Paris, France
[e] Lamarr Institute for Machine Learning and Artificial Intelligence, Dortmund, Germany
[f] Universidad Nacional Autónoma de Honduras, Tegucigalpa, Honduras
[g] Università di Bari, Bari, Italy
[h] Università di Bergamo, Bergamo, Italy
[i] Università di Bologna, Bologna, Italy
[j] Università di Cagliari, Cagliari, Italy
[k] Università di Ferrara, Ferrara, Italy
[l] Università di Firenze, Firenze, Italy
[m] Università di Genova, Genova, Italy
[n] Università degli Studi di Milano, Milano, Italy
[o] Università degli Studi di Milano-Bicocca, Milano, Italy
[p] Università di Padova, Padova, Italy
[q] Università di Perugia, Perugia, Italy
[r] Scuola Normale Superiore, Pisa, Italy

JHEP07(2025)198

[s] *Università di Pisa, Pisa, Italy*
[t] *Università della Basilicata, Potenza, Italy*
[u] *Università di Roma Tor Vergata, Roma, Italy*
[v] *Università di Siena, Siena, Italy*
[w] *Università di Urbino, Urbino, Italy*
[x] *Universidad de Ingeniería y Tecnología (UTEC), Lima, Peru*
[y] *Universidad de Alcalá, Alcalá de Henares, Spain*
[z] *Facultad de Ciencias Fisicas, Madrid, Spain*
[*] *Corresponding author*
[†] *Deceased*

JHEP07(2025)198